Enhanced self-phase modulation in silicon nitride nanowires with integrated graphene oxide 2D films

David Moss (dmoss@swin.edu.au)
Swinburne University of Technology

Research Article

Keywords: Nonlinear optics, integrated waveguides, self-phase modulation, graphene oxide

Posted Date: April 18th, 2022

DOI: https://doi.org/10.21203/rs.3.rs-1563076/v1

Abstract

We experimentally demonstrate enhanced self-phase modulation (SPM) in silicon nitride (Si_3N_4) waveguides integrated with 2D graphene oxide (GO) films. GO films are integrated onto Si_3N_4 waveguides using a solution-based, transfer-free coating method that enables precise control of the film thickness. Detailed SPM measurements are carried out using both picosecond and femtosecond optical pulses. Owing to the high Kerr nonlinearity of GO, the hybrid waveguides show significantly improved spectral broadening compared to the uncoated waveguide, achieving a broadening factor of up to ~ 3.4 for a device with 2 layers of GO. By fitting the experimental results with theory, we obtain an improvement in the waveguide nonlinear parameter by a factor of up to 18.4 and a Kerr coefficient (n_2) of GO that is about 5 orders of magnitude higher than Si_3N_4. Finally, we provide a theoretical analysis for the influence of GO film length, coating position, and its saturable absorption on the SPM performance. These results verify the effectiveness of on-chip integrating 2D GO films to enhance the nonlinear optical performance of Si_3N_4 devices.

Introduction

Self-phase modulation (SPM) is a fundamental third-order nonlinear optical process that occurs when an optical pulse travelling in a nonlinear medium, where a varying refractive index of the medium is induced by the Kerr effect, thus produces a phase shift that leads to a change in the pulse's spectrum [1-3]. It has been widely used as a relevant all-optical modulation technology for a variety of applications in broadband optical sources [4, 5], optical spectroscopy [6, 7], pulse compression [8, 9], optical logic gates [10, 11], optical modulators / switches [12, 13], optical diodes [14, 15], and optical coherence tomography [16, 17].

The ability to realize SPM based on-chip integrated photonic devices will reap attractive benefits of compact footprint, high stability, high scalability, and low-cost mass production [18-21]. Although silicon (Si) has been a dominant device platform for integrated photonics [22-24], its strong two-photon absorption (TPA) at near-infrared wavelengths leads to a low nonlinear figure-of-merit (FOM = n_2 / ($\lambda\beta_{TPA}$), where n_2 is the Kerr nonlinearity, β_{TPA} is the two photon absorption coefficient, and λ the wavelength) of ~0.3 [25], which significantly limits the SPM performance of Si devices in the telecom band. To address this, other complementary metal-oxide-semiconductor (CMOS) compatible integrated platforms such as silicon nitride (Si_3N_4) and high-index doped silica glass (Hydex) have been exploited for nonlinear optics due to their negligible TPA in this wavelength range, which yields nonlinear FOMs >>1 [26-28]. Nevertheless, their low intrinsic Kerr nonlinearity (n_2 = ~2.6 × 10^{-19} m^2 W^{-1} and ~1.3 × 10^{-19} m^2 W^{-1} for Si_3N_4 and Hydex, respectively, over an order of magnitude lower than Si [27, 29]) still poses a fundamental limitation with respect to the nonlinear efficiency [30, 31].

Recently, the on-chip integration of two-dimensional (2D) materials with ultrahigh Kerr nonlinearity has proven to be an effective way to overcome the limitations of these existing platforms and improve their

nonlinear optical performance [32-35]. Enhanced SPM has been demonstrated in integrated waveguides incorporating graphene [36-38], MoS_2 [39], WS_2 [40], and graphene oxide (GO) [41]. Amongst the different 2D materials, GO has shown many advantages for implementing hybrid integrated photonic devices with superior SPM performance, including a large Kerr nonlinearity (about 4 orders of magnitude higher than Si [42, 43]), relatively low loss compared to other 2D materials (over 2 orders of magnitude lower than graphene [44, 45]), facile synthesis processes [46, 47], and high compatibility with CMOS fabrication [48, 49]. In our previous work [41], we demonstrated enhanced SPM of picosecond optical pulses in Si waveguides integrated with 2D GO films, achieving a maximum spectral broadening factor (BF) of ~4.3 and enhanced FOM by up to 20 times.

In this paper, we demonstrate significantly improved SPM performance for Si_3N_4 waveguides integrated with 2D GO films. By using a solution-based, transfer-free coating method, we achieve on-chip integration of GO films with precise control of their thicknesses. We perform SPM measurements using both picosecond and femtosecond optical pulses centered at telecom wavelengths. Compared to the uncoated Si_3N_4 waveguide, the GO-coated waveguides show more significant spectral broadening for both the picosecond and femtosecond optical pulses, achieving a maximum BF of ~3.4 for a device with 2 layers of GO. We also fit the SPM experimental results with theory and obtain a Kerr coefficient (n_2) for GO that is about 5 orders of magnitude higher than Si_3N_4. Finally, we discuss the influence of GO film's length, coating position, and saturable absorption on the SPM performance. For Si waveguides the main challenge is to enhance the nonlinear FOM, whereas for Si_3N_4 waveguides the challenge is to enhance the nonlinear parameter g (= $2\pi n_2 / (\lambda A_{eff})$, where A_{eff} is the effective mode area) since their FOM is very large already. We obtain an enhancement in g by a factor of up to ~18.4 for a Si_3N_4 waveguide coated with 2 layers of GO, compared to the uncoated waveguide, accompanied by only a modest increase in the linear loss of about 3 dB/cm per layer of GO and with no measurable decrease in the nonlinear FOM. These results confirm the high nonlinear optical performance of Si_3N_4 waveguides integrated with 2D GO films.

Device Fabrication And Characterization

Fig. 1(a) shows a schematic of a GO-coated Si_3N_4 waveguide with a monolayer GO film. The bare Si_3N_4 waveguide has a cross-section of 1.6 μm × 0.66 μm, which was fabricated via a CMOS-compatible annealing-free and crack-free method [50, 51]. First, two-step deposition of Si_3N_4 film (330-nm-thick layer in each step) was achieved via low-pressure chemical vapor deposition (LPCVD) for strain management and crack prevention. Next, 248-nm deep ultraviolet lithography and $CF_4/CH_2F_2/O_2$ fluorine-based dry etching were employed for patterning the low-loss Si_3N_4 waveguides. A silica upper cladding was then deposited using high-density plasma-enhanced chemical vapor deposition (HDP-PECVD), followed by opening a window on it down to the top surface of the Si_3N_4 waveguides via lithography and reactive ion etching (RIE). Finally, the 2D layered GO film was coated onto the Si_3N_4 waveguide by using a solution-based method that enabled transfer-free and layer-by-layer film coating, as reported previously [45-47, 49].

Compared to the sophisticated film transfer processes employed for on-chip integration of other 2D materials such as graphene and TMDCs [38, 39, 52], our GO coating method is highly scalable, enabling precise control of the GO layer number (i.e., film thickness), large-area film coating, and good film attachment on integrated chips [43, 47]. Figs. 1(b-i) and (b-ii) show a schematic cross section and the transverse electric (TE) mode profile of the GO-coated Si_3N_4 waveguide in Fig. 1(a), respectively. The interaction between light and the GO film possessing an ultrahigh Kerr nonlinearity can be excited by the waveguide evanescent field, which underpins the enhancement of the SPM response in the hybrid waveguide.

Fig. 1(c) shows a microscope image of a Si_3N_4 integrated chip uniformly coated with a monolayer GO film, where the coated GO film exhibits good morphology, high transmittance, and high uniformity. The opened window on the silica upper cladding of the uncoated Si_3N_4 chip enables control of the film length and placement of the GO film that are in contact with the Si_3N_4 waveguide. Note that this can also be realized by patterning GO films on planarized Si_3N_4 waveguides (without silica upper cladding) via lithography and lift-off processes, as we did in our previous work [44]. In this work, we used Si_3N_4 waveguides with opened windows mainly because they have lower coupling loss and propagation loss, which is beneficial for boosting the nonlinear response of SPM.

Figs. 1(d-i) and (d-ii) show the measured Raman spectra of a Si_3N_4 chip before and after coating 2 layers of GO, respectively, where the presence of the representative D and G peaks of GO in the latter one verifies the successful on-chip integration of the GO film [44, 46]. According to our previous measurements [41, 44, 45], the GO film thickness shows a near linear relationship with layer number at small film thickness (i.e., layer numbers < 100), and the thickness for 1 layer of GO is ~2.0 nm. For the GO-coated Si_3N_4 waveguides used in the following SPM measurements, the measured film thicknesses for 1 and 2 layers of GO are ~2.1 nm and ~ 4.3 nm, respectively.

Loss Measurements

Fig. 2 shows the experimental setup used for measuring both loss and SPM of GO-coated Si_3N_4 waveguides. Three different laser sources were employed, including a tunable continuous-wave (CW) laser and two different fiber pulsed lasers (FPLs) that can generate nearly Fourier-transform limited picosecond (pulse duration: ~1.9 ps) and femtosecond optical pulses (pulse duration: ~180 fs) centered at telecom wavelengths. An optical isolator was inserted after the laser source to prevent the reflected light from damaging it. A variable optical attenuator (VOA) and a polarization controller (PC) were used to tune the power and polarization of the input light, respectively. For both the loss and SPM measurements, TE polarization of input light injected into the device under test (DUT) was chosen because it supports in-plane interaction between the waveguide evanescent field and the 2D GO film, which is much stronger compared to the out-of-plane interaction given the significant optical anisotropy of 2D materials [32, 45]. We used inverse-taper couplers at both ends of the Si_3N_4 waveguide, which were butt coupled to lensed fibers to achieve light coupling into and out of the DUT.

For the loss measurements, the power of the light before and after passing the DUT was measured by two optical power meters, i.e., OPM 1 and OPM 2. All the three laser sources were used to measure the loss of bare and GO-coated Si_3N_4 waveguides. The corresponding results are compared in Fig. 3.

Fig. 3(a) shows the insertion loss (IL_{CW}) of GO-coated Si_3N_4 waveguides versus input CW light power. Unless otherwise specified, the input power of CW light or optical pulses in this paper represents the power coupled into the waveguide after excluding the fiber-to-chip coupling loss. We measured the hybrid waveguides with 1 and 2 layers of GO (i.e., layer number $N = 1, 2$), and the corresponding results for the uncoated Si_3N_4 waveguide ($N = 0$) are also shown for comparison. The total length of the Si_3N_4 waveguide was 20 mm and the length of the opened window was 1.4 mm. The opened window started at 0.7 mm after the light input port.

As can be seen, the insertion loss does not show any obvious variation with the power of the input CW light, reflecting that the power-dependent loss induced by the photo-thermal changes in the GO films is negligible. This is because the photo-thermal changes are sensitive to the average light power coupling into the GO-coated waveguides [44, 48], and the average power of the input CW light here (< 7 mW) is much lower than those inducing significant photo-thermal changes (> 40 mW) in previous work [44, 48, 53].

According to the results in Fig. 3(a), the excess propagation losses induced by the GO films are ~3.0 dB/cm and ~6.1 dB/cm for the hybrid waveguides with 1 and 2 layers of GO, respectively. These values are slightly higher than those of GO-coated dope silica waveguides [45, 46] but lower than those of GO-coated Si waveguides [41], mainly due to the moderate GO mode overlap in the GO-coated Si_3N_4 waveguides. It is also worth mentioning that the GO-induced excess propagation loss is about 100 times lower than graphene-induced excess propagation loss in graphene-coated Si_3N_4 waveguides [51, 54], highlighting the low material absorption of GO compared to graphene and its advantage for implementing nonlinear photonic devices with relatively low loss. The low loss of GO is mainly induced by its large bandgap, which is typically between 2.1 eV – 3.6 eV [43, 55, 56]. In principle, GO with a bandgap > 2 eV has negligible linear absorption below its bandgap, e.g., at near-infrared wavelengths (with a photon energy of ~0.8 eV at 1550 nm). The light absorption of practical GO films is mainly caused by defects as well as scattering loss stemming from imperfect layer contact and film unevenness [41, 44, 45].

Figs. 3(b-i) and 3(b-ii) show the insertion loss (IL_{pulse}) of GO-coated Si_3N_4 waveguides versus input power of picosecond and femtosecond optical pulses, respectively. In contrast to CW light that has a peak power equaling to its average power, picosecond and femtosecond optical pulses have peak powers that are much higher than their average powers. Both the picosecond and femtosecond FPLs we used had the same repetition rate of ~60 MHz. For the picosecond pulses, the average input power ranged between 0.8 mW and 2.3 mW, which corresponded to a peak power range of 7 W – 20 W. For the femtosecond pulses, the average input power ranged between 1.1 mW and 1.7 mW, which corresponded to a peak power range of 98 W – 160 W. Given that the average powers of the picosecond and femtosecond optical pulses are

in the same level as that of the CW light in Fig. 3(a), the photo-thermal changes in the GO films can be neglected when these optical pulses go through the hybrid waveguides.

In both Figs. 3(b-i) and 3(b-ii), the measured IL_{pulse} of GO-coated Si_3N_4 waveguides decreases with the input power of optical pulses, and the waveguide with 2 layers of GO shows a more obvious decrease than the waveguide with 1 layer of GO. In contrast, the result for the uncoated Si_3N_4 waveguide does not show such a trend. This indicates that there is saturable absorption (SA) induced by the GO films in the hybrid waveguides. Similar phenomenon has also been observed for the GO-coated Si waveguides [41] and graphene-coated Si_3N_4 waveguides [51]. In our experiment, we also note that the change in the loss of the hybrid waveguides was not permanent, and the measured IL_{pulse} in Fig. 3(b) is repeatable.

Fig. 3(c) depicts the SA-induced excess propagation loss (ΔSA, after excluding the linear propagation loss) versus the peak power of the input optical pulses, which is extracted from the results in Figs. 3 (a) and (b). The negative values of ΔSA indicate that the loss decreases with light power, showing an opposite trend to TPA where the loss increases with light power [25, 33, 57]. The decreased loss induced by SA can facilitate more significant SPM driven by a high optical power. For femtosecond pulses, the decrease in loss is more significant than that for picosecond pulses, which can be attributed to their relatively high peak power that induces more significant SA in the GO.

Spm Measurements

In the SPM measurements, we used the same FPLs and the same fabricated devices as those employed for loss measurements in Section III to measure the SPM-induced spectral broadening. As shown in Fig. 2, picosecond or femtosecond optical pulses generated by these FPLs were coupled into the DUT, and the output signal was sent to an optical spectrum analyzer (OSA) for observation of spectral broadening. The corresponding results for the picosecond and femtosecond optical pulses are compared in Figs. 4 and 5, respectively.

Fig. 4(a) shows the normalized spectra of picosecond optical pulses before and after propagation through the uncoated and GO-coated Si_3N_4 waveguides. The peak power of the input picosecond optical pulses was kept the same at ~20 W. The output spectrum from the uncoated Si_3N_4 waveguide shows slight spectral broadening compared to the input pulse spectrum, which is mainly induced by the SPM in the Si_3N_4 waveguide. In contrast, the output spectra after propagating through the GO-coated Si_3N_4 waveguides show more significant spectral broadening, reflecting the enhanced SPM in these hybrid waveguides.

Fig. 4(b) shows the output spectra after propagation through the hybrid waveguide with 2 layers of GO measured using picosecond optical pulses with different peak powers. We chose 6 different input peak powers ranging from 7 W to 20 W – the same as those in Fig. 3(b-i). As expected, the spectral broadening of the output spectra becomes more significant as the peak power increases.

To quantitively compare the spectral broadening in these waveguides, we calculated the BFs for the measured output spectra. The BF is defined as [37, 41, 51]:

$$BF=\frac{\Delta\omega_{rms}}{\Delta\omega_0} \quad (1)$$

where $\Delta\omega_0$ and $\Delta\omega_{rms}$ are the root-mean-square (RMS) spectral widths of the input and output signals, respectively.

Fig. 4(c) shows the BFs for the uncoated and GO-coated Si_3N_4 waveguides versus the peak power of input picosecond optical pulses. As can be seen, the BFs for the GO-coated Si_3N_4 waveguides are higher than that of the uncoated waveguide, and the BF for the hybrid waveguide with 2 layers of GO is higher than that for the device with 1 layer of GO, showing agreement with the results in Fig. 4(a). The BF increases with the peak power of the optical pulses, which is consistent with the results in Fig. 4(b). At a peak power of ~20 W, a maximum BF of ~1.3 is achieved for the hybrid waveguide with 2 layers of GO.

Fig. 5(a) shows the normalized spectra of femtosecond optical pulses before and after propagation through the uncoated and GO-coated Si_3N_4 waveguides, which were measured at the same input peak power of ~160 W. Similar to Fig. 4(a), the output spectra after passing through the hybrid waveguides show more significant spectral broadening compared to the uncoated waveguide. Fig. 5(b) shows the output spectra measured at different input peak powers for the hybrid waveguide with 2 layers of GO, showing the similar trend as that in Fig. 4(b). The peak power of the input femtosecond optical pulses ranged from 98 W to 160 W – the same as those in Fig. 3(b-ii). The calculated BFs for the uncoated and GO-coated Si_3N_4 waveguides versus the input peak power are shown in Fig. 5(c). A maximum BF of ~3.4 is achieved at a peak power of 160 W for the hybrid waveguide with 2 layers of GO, which is ~2.6 times higher than the maximum BF achieved for the picosecond optical pulses. This mainly results from the relatively high peak power of the femtosecond optical pulses that drives more significant SPM in the hybrid waveguide.

Theoretical Analysis And Discussion

Based on the theory in Refs. [21, 41, 58], we simulated the evolution of optical pulses traveling along the GO-coated Si_3N_4 waveguides using the nonlinear Schrodinger equation as follows:

$$\frac{\partial A}{\partial z}=-\frac{i\beta_2}{2}\frac{\partial^2 A}{\partial t^2}+i\gamma|A|^2A-\frac{1}{2}\alpha A \quad (2)$$

where $i=\sqrt{1}$, $A(z, t)$ is the slowly varying temporal pulse envelope along the propagation direction z, β_2 is the second-order dispersion coefficient, and γ is the waveguide nonlinear parameter. The overall loss factor α includes both the linear propagation loss and the SA-induced excess propagation loss that are discussed in Fig. 3.

Unlike in Refs. [41, 58], there are no free carrier absorption (FCA) and free carrier dispersion (FCD) items in Eq. (2) since the TPA in both Si_3N_4 and GO (with bandgaps > 2 eV) is negligible at near-infrared wavelengths. We retain only the second-order dispersion item in Eq. (2) because the physical length of the waveguides (20 mm) is much smaller than the dispersion length (> 1 m) [59]. In our simulation, we divided the GO-coated Si_3N_4 waveguides into uncoated (with silica cladding) and hybrid segments (coated with 1.4-mm-long GO films). Numerically solving Eq. (2) was performed for each segment, and the output from the previous segment was set as the input for the subsequent one.

Figs. 6(a) and (b-i) show the measured and fit spectra of the input picosecond pulses and the output signal after propagation through the uncoated Si_3N_4 waveguide, respectively. The simulated spectrum evolution of the input optical pulses propagating along the uncoated waveguide is shown in Fig. 6(b-ii). The peak power of the input picosecond pulses is ~20 W. The fit spectra and spectrum evolution were calculated based on Eq. (2), which show good agreement with the experimental results. The slight discrepancies between the measured and fit spectra mainly result from imperfections of the input pulse spectrum. The fit γ for the uncoated Si_3N_4 waveguide is ~1.5 $W^{-1}m^{-1}$ – in agreement with the reported values in previous literature [20, 44, 60].

Figs. 6(c-i) and (d-i) show the measured and fit spectra for the output signals after transmission through the hybrid waveguides with 1 and 2 layers of GO, respectively. The input peak power is the same as that in Fig. 6(b). The corresponding spectrum evolutions along the hybrid waveguides are shown in Figs. 6(c-ii) and (d-ii). As can be seen, the theoretical simulations also agree well with the experimental results. The fit γ's for the hybrid waveguides with 1 and 2 layers of GO are ~11.5 and ~27.6, respectively, which are ~7.7 and ~18.4 times that of the uncoated Si_3N_4 waveguide, reflecting the significantly improved Kerr nonlinearity for the hybrid waveguides. The significant Kerr nonlinearity is also confirmed by the dramatical spectral broadening within the GO-coated region, as shown in the insets of Figs. 6(c-ii) and (d-ii).

Similar to Fig. 6, we also performed simulations based on Eq. (2) to fit the experimental results of femtosecond optical pulses. The measured and fit spectra of the input femtosecond pulses and the output signal after propagation through the uncoated Si_3N_4 waveguide are shown in Figs. 7(a) and (b-i) respectively. Figs. 7(c-i) and (d-i) show the measured and fit spectra for the output femtosecond signals after transmission through the hybrid waveguides with 1 and 2 layers of GO, respectively. The simulated spectrum evolution of the input pulses corresponding to Figs. 7(b-i), 7(c-i), and 7(d-i) are shown in Figs. 7(b-ii), 7(c-ii), and 7(d-ii), respectively. In all of these figures, the peak power of the input femtosecond pulses is ~160 W. As can be seen, all the theoretical curves show good agreement with the experimental ones. The fit γ for the uncoated Si_3N_4 waveguide and the hybrid waveguides with 1 and 2 layers of GO are the same as those obtained by fitting the experimental results of picosecond optical pulses in Fig. 6, highlighting the high consistency and further confirming the enhanced Kerr nonlinearity for the hybrid waveguides. Similar to the insets of Figs. 6(c-ii) and (d-ii), there is also dramatical spectral broadening within the GO-coated region in the insets of Figs. 7(c-ii) and (d-ii).

Based on the fit γ's of the hybrid waveguides, we further extract the Kerr coefficient (n_2) of the layered GO films using [46, 61, 62] :

$$\gamma = \frac{2\pi}{\lambda_c} \frac{\iint_D n_0^2(x,y) n_2(x,y) S_z^2 dx dy}{\left[\iint_D n_0(x,y) S_z dx dy\right]^2} \qquad (3)$$

where λ_c is the pulse central wavelength, D is the integral of the optical fields over the material regions, S_z is the time-averaged Poynting vector calculated using mode solving software, n_0 (x, y) is the refractive index profiles calculated over the waveguide cross section and n_2 (x, y) is the Kerr coefficient of the different material regions. The values of n_2 for silica and Si_3N_4 used in our calculation were 2.60×10^{-20} m^2 W^{-1} [27] and 2.59×10^{-19} m^2 W^{-1}, respectively, with the latter obtained by fitting the experimental results for the uncoated Si_3N_4 waveguide.

The fit γ's of the hybrid waveguides with 1 and 2 layers of GO are ~11.5 $W^{-1}m^{-1}$and ~27.6 $W^{-1}m^{-1}$, respectively, which are ~7.7 and ~18.4 times that of the uncoated Si_3N_4 waveguide. The extracted n_2 of 1 and 2 layers of GO are ~1.23×10^{-14} m^2 W^{-1} and ~1.19×10^{-14} m^2 W^{-1}, respectively. Both of the values are about 5 orders of magnitude higher than that of Si_3N_4 and agree reasonably well with our previous measurements [44]. Note that the n_2 of 1 layer of GO is higher than that of 2 layers of GO. We infer this may result from the increased inhomogeneous defects within the GO layers and imperfect contact between the multiple GO layers. Nonetheless, the higher GO mode overlap for the thicker 2-layer film, compared to the single-layer film, resulted in a more than doubling of the nonlinear parameter γ.

Based on the SPM modeling in Eq. (2) and the fit parameters obtained from Figs. 6 and 7, we further investigate the influence of GO film length (L_c) and coating position (L_0) on the SPM performance of GO-coated Si_3N_4 waveguides.

Figs. 8(a) and (b) show the calculated BFs versus L_c and input peak power (P_{peak}) for picosecond and femtosecond optical pulses after propagation through the hybrid waveguides, respectively. In each figure, (i) and (ii) show the results for the waveguides with 1 and 2 layers of GO, respectively. The coating position is fixed at L_0 = 0.7 mm — the same as those of the fabricated devices in Sections III and IV. The black points mark the parameters corresponding to the SPM measurements in Section IV, where the calculated BFs are consistent with the experimental results in Figs. 4 and 5. The BF increases with both L_c and P_{peak}, with maximum BFs of 4.2 (at L_c = 19.3 mm and P_{peak} = 30 W) and 25.0 (at L_c = 19.3 mm and P_{peak} = 240 W) being achieved for the picosecond and femtosecond optical pulses, respectively. This reflects that there is a large room for improvement in the SPM-induced spectral broadening by increasing the GO film length and the input peak power. The BF can also be improved by coating thicker GO films (i.e., $N > 2$), which was used for increasing the FWM conversion efficiency in Ref. [44]. The increased GO film thickness will also lead to loss increase for the hybrid waveguides and hence creates a need to balance the trade-off between the Kerr nonlinearity and loss [30, 31].

Figs. 8(c) and (d) show the calculated BFs versus L_0 and P_{peak} for picosecond and femtosecond optical pulses after propagation through the hybrid waveguides, respectively, where the film length is fixed at L_c = 1.4 mm. The simulation results marked by the black points also agree well with the experimental results in Figs. 4 and 5. The BF increases with P_{peak} – a trend similar to that in Figs. 8(a) and (b). In contrast, it decreases with L_0, with the maximum value being achieved at L_0 = 0. This indicates that the largest spectral broadening can be achieved by coating GO films at the beginning, as expected since the light power is highest at the start of the waveguide.

As discussed in Section III, the decreased loss induced by the SA in the GO films affects the SPM performance. In Figs. 9(a) and (b), we show the influence of the SA on the spectral broadening of picosecond and femtosecond optical pulses after propagation through the hybrid waveguide with 2 layers of GO, respectively. In each figure, the solid curve shows the result when considering the SA that induces a slightly reduced loss, whereas the dashed curve shows the result that was calculated using a constant linear loss of GO measured at low CW powers (i.e., the loss in Fig. 3(a)). As can be seen, the SA of GO has a positive influence and yields more significant spectral broadening for both the picosecond and femtosecond optical pulses. The difference for the femtosecond pulses is more obvious, showing a similar trend to the results for the loss decrease in Fig. 3(b) and reflecting that there is a more significant influence of the SA on the spectral broadening for optical pulses with higher peak powers.

In Table I, we provide comparisons for the parameters of the GO-Si_3N_4 waveguides in this work and the GO-Si waveguides in Ref. [41]. We note that the trade-offs and challenges involved with integrating GO films into these two very different platforms, are in turn very different. Compared to the GO-Si waveguides, GO-Si_3N_4 waveguides have a larger waveguide geometry, which results in lower mode overlap with GO films. Such a reduced GO mode overlap yields a lower GO-induced excess propagation loss, at the expense of a weaker light-GO interaction. Despite this, the nonlinear parameter γ of the GO-Si_3N_4 waveguide with 1 layer of GO is still ~7.7 times that of the uncoated waveguide. In contrast, there is only about a 2-fold improvement in the γ of the GO-Si waveguide with 1 layer of GO. This mainly due to the relatively low n_2 of Si_3N_4 compared to Si, reflecting that integrating GO onto Si_3N_4 waveguides has a more dramatic impact on improving the nonlinear performance. In contrast to Si that has strong TPA at near infrared wavelengths, the TPA of Si_3N_4 in this wavelength range is absent, which yields much higher values of nonlinear FOM for both the uncoated and GO-coated Si_3N_4 waveguides. Hence, the motivation in integrating GO films onto Si waveguides lies very much in increasing the nonlinear FOM, whereas for Si_3N_4 waveguides, the main benefit of integrating GO films is to increase the nonlinearity (i.e., nonlinear parameter γ) without introducing additional nonlinear loss.

TABLE I.

comparison of GO-coated Si_3N_4 and Si waveguides

Parameters	Si	Si_3N_4
Refractive index [a]	3.48	1.99
n_2 [a] (m^2/W)	6×10^{-18}	2.59×10^{-19}
Waveguide dimension (μm)	0.50 × 0.22	1.60 × 0.66
Waveguide length (mm)	3.0	20.0
GO film length (mm)	2.2	1.4
Waveguide propagation loss (dB/cm)	4.3	0.5
Excess propagation loss of 1 layer of GO (dB/cm)	20.5	3.0
γ_{WG} [b] ($W^{-1}m^{-1}$)	288.0	1.5
γ_{hybrid} [c] ($W^{-1}m^{-1}$)	668.0 ($N = 1$)	11.5 ($N = 1$)
	990.0 ($N = 2$)	27.6 ($N = 2$)
Fit n_2 of GO ($\times 10^{-14}$ m^2/W)	1.42 ($N = 1$)	1.23 ($N = 1$)
	1.33 ($N = 2$)	1.19 ($N = 2$)
FOM [d]	1.1 ($N = 1$) 2.4 ($N = 2$)	>>1
Ref.	[41]	This work

[a] These values are at 1550 nm.

[b] γ_{WG}: nonlinear parameters of the bare waveguides.

[c] γ_{hybrid}: nonlinear parameters of the hybrid waveguides with 1 and 2 layers of GO.

[d] The definition of $FOM = n_2 / (\lambda \beta_{TPA})$ is the same as those in Refs. [25,27], with n_2 and β_{TPA} denoting the effective Kerr coefficient and TPA coefficient of the waveguides, respectively, and λ the light wavelength at 1550 nm.

Finally, our observation of SA in the GO-coated Si_3N_4 waveguides effectively equates to having a negative nonlinear FOM, and so the very concept and utility of introducing a FOM, as first proposed [63], arguably does not apply here. For both the Si and Si_3N_4 platforms, reducing the GO film loss further through improved fabrication and integration methods (e.g., by using GO solutions with improved purity and optimized flake sizes) will directly benefit the nonlinear performance of all devices that incorporate GO films. This work demonstrates that GO, with its high nonlinearity and nonlinear FOM and relatively low loss, is an extremely interesting and attractive material to enhance the nonlinear performance of photonic chips for many applications, including Kerr microcombs and their use for microwave and RF photonics [64-218], integrated nonlinear optics [219-238] and integrated quantum optics [239-251].

Conclusion

We experimentally demonstrate enhanced SPM in Si_3N_4 waveguides integrated with 2D GO films. The integration of GO films is achieved by using a solution-based, transfer-free coating method with precise control of the film thickness. SPM measurements are performed using both picosecond and femtosecond optical pulses. The GO-coated Si_3N_4 waveguides show more significant spectral broadening than the uncoated waveguide, with a maximum BF of ~3.4 being achieved for a device with 2 layers of GO. The

experimental results show good agreement with theory, achieving up to ~18.4 times improvement in the waveguide nonlinear parameter compared to uncoated waveguide and a fit n_2 of GO that is about 5 orders of magnitude higher than Si_3N_4. Analysis for the influence of GO film's length, coating position, and SA on the SPM performance is also provided. This work demonstrates that the Si_3N_4 can be effectively transformed into a highly performing CMOS-compatible nonlinear photonic platform by integrating 2D GO films.

Declarations

Competing interests: The authors declare no competing interests.

References

[1] R. Stolen and C. Lin, "Self-phase-modulation in silica optical fibers," *Phys. Rev. A,* vol. 17, no. 4, pp. 1448, Apr. 1978.

[2] G. Agrawal and N. Olsson, "Self-phase modulation and spectral broadening of optical pulses in semiconductor laser amplifiers," *IEEE J Quantum Electron.,* vol. 25, no. 11, pp. 2297-2306, Nov. 1989.

[3] L. Wu *et al.*, "Recent advances of spatial self-phase modulation in 2D materials and passive photonic device applications," *Small,* vol. 16, no. 35, pp. 2002252, Jul. 2020.

[4] H. Guo *et al.*, "Mid-infrared frequency comb via coherent dispersive wave generation in silicon nitride nanophotonic waveguides," *Nat. Photonics,* vol. 12, no. 6, pp. 330-335, Jun. 2018.

[5] Y. Yu *et al.*, "A broadband, quasi-continuous, mid-infrared supercontinuum generated in a chalcogenide glass waveguide," *Laser Photonics Rev.,* vol. 8, no. 5, pp. 792-798, May 2014.

[6] J. Hult, R. Watt, and C. Kaminski, "High bandwidth absorption spectroscopy with a dispersed supercontinuum source," *Opt. Express,* vol. 15, no. 18, pp. 11385-11395, Aug. 2007.

[7] K. Kaltenecker *et al.*, "Near-infrared nanospectroscopy using a low-noise supercontinuum source," *APL Photonics,* vol. 6, no. 6, pp. 066106, Jun. 2021.

[8] N. Krebs, I. Pugliesi, and E. Riedle, "Pulse compression of ultrashort UV pulses by self-phase modulation in bulk material," *Appl. Sci.,* vol. 3, no. 1, pp. 153-167, Feb. 2013.

[9] M. Peccianti *et al.*, "Subpicosecond optical pulse compression via an integrated nonlinear chirper," *Opt. Express,* vol. 18, no. 8, pp. 7625-7633, Apr. 2010.

[10] L. Wu *et al.*, "1D@ 0D hybrid dimensional heterojunction-based photonics logical gate and isolator," *Appl. Mater. Today,* vol. 19, pp. 100589, Jun. 2020.

[11] P. Singh, D. Tripathi, S. Jaiswal, and H. Dixit, "All-optical logic gates: designs, classification, and comparison," *Adv. Opt. Technol.,* 2014. Article ID: 275083

[12] L. Wu *et al*., "2D tellurium based high-performance all-optical nonlinear photonic devices," *Adv. Func. Mater.,* vol. 29, no. 4, pp. 1806346, Nov. 2019.

[13] L. Wu *et al*., "2D MXene: MXene-based nonlinear optical information converter for all-optical modulator and switcher," *Laser Photonics Rev.,* vol. 12, no. 12, pp 1870055, Oct. 2018.

[14] Y. Dong *et al*., "Saturable absorption in 2D Ti3C2 MXene thin films for passive photonic diodes," *Adv. Mater.,* vol. 30, no. 10, pp. 1705714, Jan. 2018.

[15] S. Konorov *et al*., "Experimental demonstration of a photonic-crystal-fiber optical diode," *Appl. Phys. B,* vol. 78, no. 5, pp. 547-550, Mar. 2004.

[16] S. Moon and D. Kim, "Ultra-high-speed optical coherence tomography with a stretched pulse supercontinuum source," *Opt. Express,* vol. 14, no. 24, pp. 11575-11584, Nov. 2006.

[17] K. Sumimura, Y. Genda, T. Ohta, K. Itoh, and N. Nishizawa, "Quasi-supercontinuum generation using 1.06 μmultrashort-pulse laser system for ultrahigh-resolution optical-coherence tomography," *Opt. Lett.,* vol. 35, no. 21, pp. 3631-3633, Oct. 2010.

[18] E. Dulkeith, Y. Vlasov, X. Chen, N. Panoiu, and R. Osgood, "Self-phase-modulation in submicron silicon-on-insulator photonic wires," *Opt. Express,* vol. 14, no. 12, pp. 5524-5534, Jun. 2006.

[19] O. Boyraz, T. Indukuri, and B. Jalali, "Self-phase-modulation induced spectral broadening in silicon waveguides," *Opt. Express,* vol. 12, no. 5, pp. 829-834, Mar. 2004.

[20] D. Tan, K. Ikeda, P. Sun, and Y. Fainman, "Group velocity dispersion and self phase modulation in silicon nitride waveguides," *Appl. Phys. Lett.,* vol. 96, no. 6, pp. 061101, Feb. 2010.

[21] D. Duchesne *et al*., "Efficient self-phase modulation in low loss, high index doped silica glass integrated waveguides," *Opt. Express,* vol. 17, no. 3, pp. 1865-1870, Jan. 2009.

[22] W. Bogaerts and L. Chrostowski, "Silicon photonics circuit design: methods, tools and challenges," *Laser Photonics Rev.,* vol. 12, no. 4, pp. 1700237, Mar. 2018.

[23] S. Feng, T. Lei, H. Chen, H. Cai, X. Luo, and A. Poon, "Silicon photonics: from a microresonator perspective," *Laser Photonics Rev.,* vol. 6, no. 2, pp. 145-177, Aug. 2012.

[24] G. Reed, G. Mashanovich, F. Gardes, and D. Thomson, "Silicon optical modulators," *Nat. photonics,* vol. 4, no. 8, pp. 518-526, Aug. 2010.

[25] J. Leuthold, C. Koos, and W. Freude, "Nonlinear silicon photonics," *Nat. Photonics,* vol. 4, no. 8, pp. 535-544, Aug. 2010.

[26] J. Levy, A. Gondarenko, M. Foster, A. Turner-Foster, A. Gaeta, and M. Lipson, "CMOS-compatible multiple-wavelength oscillator for on-chip optical interconnects," *Nat. photonics,* vol. 4, no. 1, pp. 37-40, Jan. 2010.

[27] D. Moss, R. Morandotti, A. Gaeta, and M. Lipson, "New CMOS-compatible platforms based on silicon nitride and Hydex for nonlinear optics," *Nat. Photonics,* vol. 7, no. 8, pp. 597-607, Aug. 2013.

[28] M. Ferrera *et al.*, "Low-power continuous-wave nonlinear optics in doped silica glass integrated waveguide structures," *Nat. photonics,* vol. 2, no. 12, pp. 737-740, Dec. 2008.

[29] M. Foster, A. Turner, J. Sharping, B. Schmidt, M. Lipson, and A. Gaeta, "Broad-band optical parametric gain on a silicon photonic chip," *Nature,* vol. 441, no. 7096, pp. 960-963, Jun. 2006.

[30] Y. Qu *et al.*, "Analysis of four-wave mixing in silicon nitride waveguides integrated with 2D layered graphene oxide films," *J. Lightwave Technol.,* vol. 39, no. 9, pp. 2902-2910, May. 2021.

[31] Y. Zhang, J. Wu, Y. Qu, L. Jia, B. Jia, and D. J. Moss, "Optimizing the Kerr nonlinear optical performance of silicon waveguides integrated with 2D graphene oxide films," *J. Lightwave Technol.,* vol. 39, no. 14, pp. 4671-4683, Mar. 2021.

[32] T. Gu *et al.*, "Regenerative oscillation and four-wave mixing in graphene optoelectronics," *Nat. Photonics,* vol. 6, no. 8, pp. 554-559, Aug. 2012.

[33] A. Autere, H. Jussila, Y. Dai, Y. Wang, H. Lipsanen, and Z. Sun, "Nonlinear optics with 2D layered materials," *Adv. Mater.,* vol. 30, no. 24, pp. 1705963, Jun. 2018.

[34] W. Liu *et al.*, "Recent advances of 2D materials in nonlinear photonics and fiber lasers," *Adv. Opt. Mater.,* vol. 8, no. 8, pp. 1901631, Feb. 2020.

[35] I. Alonso Calafell *et al.*, "Giant enhancement of third-harmonic generation in graphene–metal heterostructures," *Nat. Nanotechnol.,* vol. 16, no. 3, pp. 318-324, Mar. 2021.

[36] A. Ishizawa *et al.*, "Optical nonlinearity enhancement with graphene-decorated silicon waveguides," *Sci. Rep.,* vol. 7, no. 1, pp. 45520, Apr. 2017.

[37] N. Vermeulen *et al.*, "Graphene's nonlinear-optical physics revealed through exponentially growing self-phase modulation," *Nature Commun.,* vol. 9, no. 1, pp. 2675, Jul. 2018.

[38] Q. Feng *et al.*, "Enhanced optical Kerr nonlinearity of graphene/Si hybrid waveguide," *Appl. Phys. Lett.,* vol. 114, no. 7, pp. 071104, Feb. 2019.

[39] L. Liu, K. Xu, X. Wan, J. Xu, C. Y. Wong, and H. K. Tsang, "Enhanced optical Kerr nonlinearity of MoS_2 on silicon waveguides," *Photonics Res.,* vol. 3, no. 5, pp. 206-209, Oct. 2015.

[40] Y. Wang *et al.*, "Enhancing Si_3N_4 waveguide nonlinearity with heterogeneous integration of few-layer WS_2," *ACS Photonics,* vol. 8, no. 9, pp. 2713-2721, Sep. 2021.

[41] Y. Zhang *et al.*, "Enhanced Kerr nonlinearity and nonlinear figure of merit in silicon nanowires integrated with 2D graphene oxide films," *ACS Appl. Mater. Interfaces,* vol. 12, no. 29, pp. 33094-33103, Jul. 2020.

[42] X. Zheng, B. Jia, X. Chen, and M. Gu, "In situ third-order non-linear responses during laser reduction of graphene oxide thin films towards on-chip non-linear photonic devices," *Adv, Mater.,* vol. 26, no. 17, pp. 2699-2703, May 2014.

[43] J. Wu, L. Jia, Y. Zhang, Y. Qu, B. Jia, and D. Moss, "Graphene oxide for integrated photonics and flat optics," *Adv. Mater.*, vol. 33, no. 3, pp. 200415, Jan. 2021.

[44] Y. Qu *et al.*, "Enhanced four-wave mixing in silicon nitride waveguides integrated with 2D layered graphene oxide films," *Adv. Opt. Mater.*, vol. 8, no. 20, pp. 2001048, Oct. 2020.

[45] J. Wu *et al.*, "Graphene oxide waveguide and micro-ring resonator polarizers," *Laser Photonics Rev.,* vol. 13, no. 9, pp. 1900056, Sep. 2019.

[46] Y. Yang *et al.*, "Invited article: Enhanced four-wave mixing in waveguides integrated with graphene oxide," *APL Photonics,* vol. 3, no. 12, pp. 120803, Oct. 2018.

[47] Y. Yang *et al.*, "Graphene-based multilayered metamaterials with phototunable architecture for on-chip photonic devices," *ACS Photonics,* vol. 6, no. 4, pp. 1033-1040, Apr. 2019.

[48] J. Wu *et al.*, "2D layered graphene oxide films integrated with micro-ring resonators for enhanced nonlinear optics," *Small,* vol. 16, no. 16, pp. 1906563, Apr. 2020.

[49] L. Jia *et al.*, "Fabrication technologies for the on-chip integration of 2D materials," *Small Methods,* vol. 6, no. 3, pp. 2101435, Mar. 2022.

[50] H. El Dirani *et al.*, "Annealing-free Si_3N_4 frequency combs for monolithic integration with Si photonics," *Appl. Phys. Lett.,* vol. 113, no. 8, pp. 081102, Aug. 2018.

[51] P. Demongodin *et al.*, "Ultrafast saturable absorption dynamics in hybrid graphene/Si_3N_4 waveguides," *APL Photonics,* vol. 4, no. 7, pp. 076102, Jul. 2019.

[52] Y. Yang *et al.*, "Bottom-up fabrication of graphene on silicon/silica substrate via a facile soft-hard template approach," *Sci. Rep.,* vol. 5, no. 1, pp. 1-7, Aug. 2015.

[53] Y. Zhang, J. Wu, Y. Qu, L. Jia, B. Jia, and D. Moss, "Design and optimization of four-wave mixing in microring resonators integrated with 2D graphene oxide films," *J. Lightwave Technol.*, vol. 39, no. 20, pp. 6553-6562, Oct. 2021.

[54] K. Alexander, N. Savostianova, S. Mikhailov, B. Kuyken, and D. Van Thourhout, "Electrically tunable optical nonlinearities in graphene-covered SiN waveguides characterized by four-wave mixing," *ACS Photonics,* vol. 4, no. 12, pp. 3039-3044, Dec. 2017.

[55] D. Lee, S. Na, and S. Kim, "Graphene oxide/PEDOT: PSS composite hole transport layer for efficient and stable planar heterojunction perovskite solar cells," *Nanoscale,* vol. 8, no. 3, pp. 1513-1522, Nov. 2016.

[56] S. Rafique, S. Abdullah, M. Shahid, M. Ansari, and K. Sulaiman, "Significantly improved photovoltaic performance in polymer bulk heterojunction solar cells with graphene oxide/PEDOT: PSS double decked hole transport layer," *Sci. Rep.,* vol. 7, no. 1, pp. 1-10, Jan. 2017.

[57] J. Wu *et al.*, "RF Photonics: An optical microcombs' perspective," *IEEE IEEE J Sel. Top. Quantum Electron.,* vol. 24, no. 4, pp. 1-20, Feb. 2018.

[58] L. Yin and G. Agrawal, "Impact of two-photon absorption on self-phase modulation in silicon waveguides," *Opt. Lett.,* vol. 32, no. 14, pp. 2031-2033, Jul. 2007.

[59] G. Agrawal, "Nonlinear fiber optics," 2000.

[60] H. Dirani *et al.*, "Crack-free silicon-nitride-on-insulator nonlinear circuits for continuum generation in the C-Band," *IEEE Photon. Technol. Lett.,* vol. 30, no. 4, pp. 355-358, Jan. 2018.

[61] C. Donnelly and D. Tan, "Ultra-large nonlinear parameter in graphene-silicon waveguide structures," *Opt. Express,* vol. 22, no. 19, pp. 22820-22830, Sep. 2014.

[62] M. Ji *et al.*, "Enhanced parametric frequency conversion in a compact silicon-graphene microring resonator," *Opt. Express,* vol. 23, no. 14, pp. 18679-18685, Jul. 2015.

[63] V. Mizrahi, K. DeLong, G. Stegeman, M. Saifi, and M. Andrejco, "Two-photon absorption as a limitation to all-optical switching," *Opt. Lett.,* vol. 14, no. 20, pp. 1140-1142, Oct. 1989.

[65] L. Razzari, D. Duchesne, M. Ferrera, R. Morandotti, S. Chu, B. E. Little, and D. J. Moss, "CMOS-compatible integrated optical hyper-parametric oscillator," Nature Photonics, vol. 4, no. 1, pp. 41-45, 2010/01/01, 2010.

[66] A. Pasquazi, M. Peccianti, L. Razzari, D. J. Moss, S. Coen, M. Erkintalo, Y. K. Chembo, T. Hansson, S. Wabnitz, P. Del'Haye, X. Xue, A. M. Weiner, and R. Morandotti, "Micro-combs: A novel generation of optical sources," Physics Reports, vol. 729, pp. 1-81, 2018/01/27/, 2018.

[67] P. Del'Haye, A. Schliesser, O. Arcizet, T. Wilken, R. Holzwarth, and T. J. Kippenberg, "Optical frequency comb generation from a monolithic microresonator," Nature, vol. 450, no. 7173, pp. 1214-1217, 2007/12/01, 2007.

[68] B. Corcoran, et al., “Ultra-dense optical data transmission over standard fiber with a single chip source”, Nature Communications, vol. 11, Article:2568, 2020.

[69] C.Prayoonyong et al., “Frequency comb distillation for optical superchannel transmission”, Journal of Lightwave Technology Vol. 39 (23) 7383-7392 (2021).

[70] X. Xu, M. Tan, B. Corcoran, J. Wu, T. G. Nguyen, A. Boes, S. T. Chu, B. E. Little, R. Morandotti, A. Mitchell, D. G. Hicks, and D. J. Moss, “Photonic Perceptron Based on a Kerr Microcomb for High-Speed, Scalable, Optical Neural Networks,” Laser & Photonics Reviews, vol. 14, no. 10, pp. 2000070, 2020.

[71] X. Xu, M. Tan, B. Corcoran, J. Wu, A. Boes, T. G. Nguyen, S. T. Chu, B. E. Little, D. G. Hicks, R. Morandotti, A. Mitchell, and D. J. Moss, “11 TOPS photonic convolutional accelerator for optical neural networks,” Nature, vol. 589, no. 7840, pp. 44-51, 2021/01/01, 2021.

[72] W. Wang, Z. Lu, W. Zhang, S. T. Chu, B. E. Little, L. Wang, X. Xie, M. Liu, Q. Yang, L. Wang, J. Zhao, G. Wang, Q. Sun, Y. Liu, Y. Wang, and W. Zhao, “Robust soliton crystals in a thermally controlled microresonator,” Optics Letters, vol. 43, no. 9, pp. 2002-2005, 2018/05/01, 2018.

[73] D. C. Cole, E. S. Lamb, P. Del’Haye, S. A. Diddams, and S. B. Papp, “Soliton crystals in Kerr resonators,” Nature Photonics, vol. 11, no. 10, pp. 671-676, 2017/10/01, 2017.

[74] M. Karpov, M. H. P. Pfeiffer, H. Guo, W. Weng, J. Liu, and T. J. Kippenberg, “Dynamics of soliton crystals in optical microresonators,” Nature Physics, vol. 15, no. 10, pp. 1071-1077, 2019/10/01, 2019.

[75] H. Bao, A. Cooper, M. Rowley, L. Di Lauro, J. S. Totero Gongora, S. T. Chu, B. E. Little, G.-L. Oppo, R. Morandotti, D. J. Moss, B. Wetzel, M. Peccianti, and A. Pasquazi, “Laser cavity-soliton microcombs,” Nature Photonics, vol. 13, no. 6, pp. 384-389, 2019/06/01, 2019.

[76] A. Pasquazi, M. Peccianti, B. E. Little, S. T. Chu, D. J. Moss, and R. Morandotti, “Stable, dual mode, high repetition rate mode-locked laser based on a microring resonator,” Optics Express, vol. 20, no. 24, pp. 27355-27363, 2012/11/19, 2012.

[77] A. Pasquazi, L. Caspani, M. Peccianti, M. Clerici, M. Ferrera, L. Razzari, D. Duchesne, B. E. Little, S. T. Chu, D. J. Moss, and R. Morandotti, “Self-locked optical parametric oscillation in a CMOS compatible microring resonator: a route to robust optical frequency comb generation on a chip,” Optics Express, vol. 21, no. 11, pp. 13333-13341, 2013/06/03, 2013.

[78] V. Torres-Company, and A. M. Weiner, “Optical frequency comb technology for ultra-broadband radio-frequency photonics,” Laser & Photonics Reviews, vol. 8, no. 3, pp. 368-393, 2014.

[79] M. Peccianti, A. Pasquazi, Y. Park, B. E. Little, S. T. Chu, D. J. Moss, and R. Morandotti, “Demonstration of a stable ultrafast laser based on a nonlinear microcavity,” Nature Communications, vol. 3, no. 1, pp. 765, 2012/04/03, 2012.

[80] L. Di Lauro, J. Li, D. J. Moss, R. Morandotti, S. T. Chu, M. Peccianti, and A. Pasquazi, “Parametric control of thermal self-pulsation in micro-cavities,” Optics Letters, vol. 42, no. 17, pp. 3407-3410, 2017/09/01, 2017.

[81] H. Bao, A. Cooper, S. T. Chu, D. J. Moss, R. Morandotti, B. E. Little, M. Peccianti, and A. Pasquazi, “Type-II micro-comb generation in a filter-driven four wave mixing laser [Invited],” Photonics Research, vol. 6, no. 5, pp. B67-B73, 2018/05/01, 2018.

[82] Chou, J., Han, Y., and Jalali, B.: ‘Adaptive RF-photonic arbitrary waveform generator’, IEEE Photonics Technology Letters, 2003, 15, (4), pp. 581-583

[83] X. Xue, Y. Xuan, H.-J. Kim, J. Wang, D. E. Leaird, M. Qi, and A. M. Weiner, “Programmable Single-Bandpass Photonic RF Filter Based on Kerr Comb from a Microring,” Journal of Lightwave Technology, vol. 32, no. 20, pp. 3557-3565, 2014/10/15, 2014.

[84] T. J. Kippenberg, R. Holzwarth, and S. A. Diddams, “Microresonator-Based Optical Frequency Combs,” Science, vol. 332, no. 6029, pp. 555-559, 2011.

[85] X. Xu, J. Wu, M. Shoeiby, T. G. Nguyen, S. T. Chu, B. E. Little, R. Morandotti, A. Mitchell, and D. J. Moss, “Reconfigurable broadband microwave photonic intensity differentiator based on an integrated optical frequency comb source,” APL Photonics, vol. 2, no. 9, pp. 096104, 2017.

[86] X. Xu, M. Tan, J. Wu, R. Morandotti, A. Mitchell, and D. J. Moss, “Microcomb-Based Photonic RF Signal Processing,” IEEE Photonics Technology Letters, vol. 31, no. 23, pp. 1854-1857, 2019.

[87] X. Xu, J. Wu, T. G. Nguyen, M. Shoeiby, S. T. Chu, B. E. Little, R. Morandotti, A. Mitchell, and D. J. Moss, “Advanced RF and microwave functions based on an integrated optical frequency comb source,” Optics Express, vol. 26, no. 3, pp. 2569-2583, 2018/02/05, 2018.

[88] X. Xue, Y. Xuan, C. Bao, S. Li, X. Zheng, B. Zhou, M. Qi, and A. M. Weiner, “Microcomb-Based True-Time-Delay Network for Microwave Beamforming With Arbitrary Beam Pattern Control,” Journal of Lightwave Technology, vol. 36, no. 12, pp. 2312-2321, 2018.

[89] X. Xu, J. Wu, T. G. Nguyen, S. T. Chu, B. E. Little, R. Morandotti, A. Mitchell, and D. J. Moss, “Broadband RF Channelizer Based on an Integrated Optical Frequency Kerr Comb Source,” Journal of Lightwave Technology, vol. 36, no. 19, pp. 4519-4526, 2018.

[90] X. Xu, J. Wu, M. Tan, T. G. Nguyen, S. T. Chu, B. E. Little, R. Morandotti, A. Mitchell, and D. J. Moss, “Orthogonally Polarized RF Optical Single Sideband Generation and Dual-Channel Equalization Based on an Integrated Microring Resonator,” Journal of Lightwave Technology, vol. 36, no. 20, pp. 4808-4818, 2018.

[91] X. Xu, J. Wu, T. G. Nguyen, T. Moein, S. T. Chu, B. E. Little, R. Morandotti, A. Mitchell, and D. J. Moss, “Photonic microwave true time delays for phased array antennas using a 49 GHz FSR

integrated optical micro-comb source," Photonics Research, vol. 6, no. 5, pp. B30-B36, 2018/05/01, 2018.

[92] X. Xu, M. Tan, J. Wu, T. G. Nguyen, S. T. Chu, B. E. Little, R. Morandotti, A. Mitchell, and D. J. Moss, "Advanced Adaptive Photonic RF Filters with 80 Taps Based on an Integrated Optical Micro-Comb Source," Journal of Lightwave Technology, vol. 37, no. 4, pp. 1288-1295, 2019/02/15, 2019.

[93] W. Liang, D. Eliyahu, V. S. Ilchenko, A. A. Savchenkov, A. B. Matsko, D. Seidel, and L. Maleki, "High spectral purity Kerr frequency comb radio frequency photonic oscillator," Nature Communications, vol. 6, no. 1, pp. 7957, 2015/08/11, 2015.

[94] J. Liu, E. Lucas, A. S. Raja, J. He, J. Riemensberger, R. N. Wang, M. Karpov, H. Guo, R. Bouchand, and T. J. Kippenberg, "Photonic microwave generation in the X- and K-band using integrated soliton microcombs," Nature Photonics, vol. 14, no. 8, pp. 486-491, 2020/08/01, 2020.

[95] M. Tan, X. Xu, J. Wu, R. Morandotti, A. Mitchell, and D. J. Moss, "Photonic RF and microwave filters based on 49 GHz and 200 GHz Kerr microcombs," Optics Communications, vol. 465, pp. 125563, 2020/06/15/, 2020.

[96] X. Xu, M. Tan, J. Wu, A. Boes, T. G. Nguyen, S. T. Chu, B. E. Little, R. Morandotti, A. Mitchell, and D. J. Moss, "Broadband Photonic RF Channelizer With 92 Channels Based on a Soliton Crystal Microcomb," Journal of Lightwave Technology, vol. 38, no. 18, pp. 5116-5121, 2020.

[97] X. Xu, M. Tan, J. Wu, A. Boes, B. Corcoran, T. G. Nguyen, S. T. Chu, B. E. Little, R. Morandotti, A. Mitchell, and D. Moss, "Photonic RF Phase-Encoded Signal Generation With a Microcomb Source," Journal of Lightwave Technology, vol. 38, no. 7, pp. 1722-1727, 2020.

[98] X. Xu, M. Tan, J. Wu, T. G. Nguyen, S. T. Chu, B. E. Little, R. Morandotti, A. Mitchell, and D. J. Moss, "High performance RF filters via bandwidth scaling with Kerr micro-combs," APL Photonics, vol. 4, no. 2, pp. 026102, 2019.

[99] M. Tan, X. Xu, B. Corcoran, J. Wu, A. Boes, T. G. Nguyen, S. T. Chu, B. E. Little, R. Morandotti, A. Mitchell, and D. J. Moss, "Microwave and RF Photonic Fractional Hilbert Transformer Based on a 50 GHz Kerr Micro-Comb," Journal of Lightwave Technology, vol. 37, no. 24, pp. 6097-6104, 2019.

[100] M. Tan, X. Xu, B. Corcoran, J. Wu, A. Boes, T. G. Nguyen, S. T. Chu, B. E. Little, R. Morandotti, A. Mitchell, and D. J. Moss, "RF and Microwave Fractional Differentiator Based on Photonics," IEEE Transactions on Circuits and Systems II: Express Briefs, vol. 67, no. 11, pp. 2767-2771, 2020.

[101] M. Tan, X. Xu, A. Boes, B. Corcoran, J. Wu, T. G. Nguyen, S. T. Chu, B. E. Little, R. Morandotti, A. Mitchell, and D. J. Moss, "Photonic RF Arbitrary Waveform Generator Based on a Soliton Crystal Micro-Comb Source," Journal of Lightwave Technology, vol. 38, no. 22, pp. 6221-6226, 2020/11/15, 2020.

[102] M. Tan, X. Xu, J. Wu, R. Morandotti, A. Mitchell, and D. Moss, "RF and microwave photonic temporal signal processing with Kerr micro-combs," Advances in Physics: X, vol. 6, no. 1, pp. 1-46, 2021.

[103] J. Wu, X. Xu, T. G. Nguyen, S. T. Chu, B. E. Little, R. Morandotti, A. Mitchell, and D. J. Moss, "Orthogonally polarized optical single sideband generation based on integrated microring resonators," OSA Technical Digest. p. M1B.5.

[104] Mengxi Tan, Xingyuan Xu, Jiayang Wu, Bill Corcoran, Andreas Boes, Thach G. Nguyen, Sai T. Chu, Brent E. Little, Roberto Morandotti, Arnan Mitchell, and David J. Moss, "Integral order photonic RF signal processors based on a soliton crystal micro-comb source", IOP Journal of Optics Vol. 23 (11) 125701 (2021).

[105] M. Tan, X. Xu, J. Wu, T. G. Nguyen, S. T. Chu, B. E. Little, R. Morandotti, A. Mitchell, and D. J. Moss, "Photonic Radio Frequency Channelizers based on Kerr Optical Micro-combs", IOP Journal of Semiconductors Vol. 42 (4), 041302 (2021).

[106] M. Tan, X. Xu, J. Wu, T. G. Nguyen, S. T. Chu, B. E. Little, R. Morandotti, A. Mitchell, and D. J. Moss, "Orthogonally polarized Photonic Radio Frequency single sideband generation with integrated micro-ring resonators", IOP Journal of Semiconductors, Vol. 42 (4), 041305 (2021).

[107] Xu, X., et al., Photonic microwave true time delays for phased array antennas using a 49 GHz FSR integrated micro-comb source, Photonics Research, vol. 6, B30-B36 (2018).

[108] T. G. Nguyen et al., "Integrated frequency comb source-based Hilbert transformer for wideband microwave photonic phase analysis," Opt. Express, vol. 23, no. 17, pp. 22087-22097, Aug. 2015.

[109] X. Xu, J. Wu, M. Shoeiby, T. G. Nguyen, S. T. Chu, B. E. Little, R. Morandotti, A. Mitchell, and D. J. Moss, "Reconfigurable broadband microwave photonic intensity differentiator based on an integrated optical frequency comb source," APL Photonics, vol. 2, no. 9, 096104, Sep. 2017.

[110] X. Xu, M. Tan, J. Wu, R. Morandotti, A. Mitchell, and D. J. Moss, "Microcomb-based photonic RF signal processing", IEEE Photonics Technology Letters, vol. 31 no. 23 1854-1857, 2019.

[111] X. Xu, et al., "Broadband RF channelizer based on an integrated optical frequency Kerr comb source," Journal of Lightwave Technology, vol. 36, no. 19, pp. 4519-4526, 2018.

[112] X. Xu, et al., "Continuously tunable orthogonally polarized RF optical single sideband generator based on micro-ring resonators," Journal of Optics, vol. 20, no. 11, 115701. 2018.

[113] X. Xu, et al., "Orthogonally polarized RF optical single sideband generation and dual-channel equalization based on an integrated microring resonator," Journal of Lightwave Technology, vol. 36, no. 20, pp. 4808-4818. 2018.

[114] M. Tan, X. Xu, J. Wu, A. Boes, B. Corcoran, T. G. Nguyen, S. T. Chu, B. E. Little, R. Morandotti, A. Mitchell, and D. J. Moss, "Advanced applications of Kerr mircocombs", Paper 11775-1. SPIE 11775, Integrated Optics: Design, Devices, Systems and Applications VI, (EOO21) OO107-8, Proc 1177504 (18

April 2021); Integrated Optics Conference, SPIE Optics and Optoelectronics Symposium, Prague, Czech Republic. April 19 - 22 (2021), doi.org/10.1117/12.2588733.

[115] M.Tan, X. Xu, J. Wu, B. Corcoran, A. Boes, T. G. Nguyen, Sai T. Chu, B. E. Little, R.Morandotti, A. Mitchell, and D. J. Moss, “Integral order photonic RF signal processors based on a soliton crystal micro-comb source”, IOP Journal of Optics vol. 23 (11) 125701 (2021).

[116] X. Xu, et al., “Advanced adaptive photonic RF filters with 80 taps based on an integrated optical micro-comb source,” Journal of Lightwave Technology, vol. 37, no. 4, pp. 1288-1295, 2019.

[117] X. Xu, et al., Broadband microwave frequency conversion based on an integrated optical micro-comb source”, Journal of Lightwave Technology, vol. 38 no. 2, pp. 332-338, 2020.

[118] M. Tan, et al., “Photonic RF and microwave filters based on 49GHz and 200GHz Kerr microcombs”, Optics Comm. vol. 465,125563, Feb. 22. 2020.

[119] X. Xu, et al., “Broadband photonic RF channelizer with 90 channels based on a soliton crystal microcomb”, Journal of Lightwave Technology, Vol. 38, no. 18, pp. 5116 - 5121, 2020. doi: 10.1109/JLT.2020.2997699.

[120] X. Xu, et al., “Photonic RF and microwave integrator with soliton crystal microcombs”, IEEE Transactions on Circuits and Systems II: Express Briefs, vol. 67, no. 12, pp. 3582-3586, 2020. DOI:10.1109/TCSII.2020.2995682.

[121] X. Xu, et al., “Photonic RF phase-encoded signal generation with a microcomb source”, J. Lightwave Technology, vol. 38, no. 7, 1722-1727, 2020.

[122] X. Xu, et al., “High performance RF filters via bandwidth scaling with Kerr micro-combs,” APL Photonics, vol. 4, no. 2, pp. 026102. 2019.

[123] Xu, X., et al., Photonic microwave true time delays for phased array antennas using a 49 GHz FSR integrated micro-comb source, Photonics Research, vol. 6, B30-B36 (2018).

[124] X. Xu, M. Tan, J. Wu, R. Morandotti, A. Mitchell, and D. J. Moss, “Microcomb-based photonic RF signal processing”, IEEE Photonics Technology Letters, vol. 31 no. 23 1854-1857, 2019.

[125] M. Tan et al, “Orthogonally polarized Photonic Radio Frequency single sideband generation with integrated micro-ring resonators”, IOP Journal of Semiconductors, Vol. 42 (4), 041305 (2021). DOI: 10.1088/1674-4926/42/4/041305.

[126] Xu, et al., “Advanced adaptive photonic RF filters with 80 taps based on an integrated optical micro-comb source,” Journal of Lightwave Technology, vol. 37, no. 4, pp. 1288-1295 (2019).

[127] X. Xu, et al., Broadband microwave frequency conversion based on an integrated optical micro-comb source", Journal of Lightwave Technology, vol. 38 no. 2, pp. 332-338, 2020.

[128] M. Tan, et al., "Photonic RF and microwave filters based on 49GHz and 200GHz Kerr microcombs", Optics Comm. vol. 465,125563, Feb. 22. 2020.

[129] X. Xu, et al., "Broadband photonic RF channelizer with 90 channels based on a soliton crystal microcomb", Journal of Lightwave Technology, Vol. 38, no. 18, pp. 5116 - 5121, 2020. doi: 10.1109/JLT.2020.2997699.

[130] X. Xu, et al., "Photonic RF and microwave integrator with soliton crystal microcombs", IEEE Transactions on Circuits and Systems II: Express Briefs, vol. 67, no. 12, pp. 3582-3586, 2020.

[131] X. Xu, J. Wu, M. Tan, T. G. Nguyen, S. T. Chu, B. E. Little, R. Morandotti, A. Mitchell, and D. J. Moss, "Broadband Microwave Frequency Conversion Based on an Integrated Optical Micro-Comb Source," Journal of Lightwave Technology, vol. 38, no. 2, pp. 332-338, 2020.

[132] X. Xu, et al., "High performance RF filters via bandwidth scaling with Kerr micro-combs," APL Photonics, vol. 4 (2) 026102. 2019.

[133] M. Tan, et al., "Microwave and RF photonic fractional Hilbert transformer based on a 50 GHz Kerr micro-comb", Journal of Lightwave Technology, vol. 37, no. 24, pp. 6097 – 6104, 2019.

[134] M. Tan, et al., "Photonic RF arbitrary waveform generator based on a soliton crystal micro-comb source", Journal of Lightwave Technology, vol. 38, no. 22, pp. 6221-6226 (2020). DOI: 10.1109/JLT.2020.3009655.

[135] M. Tan, X. Xu, J. Wu, R. Morandotti, A. Mitchell, and D. J. Moss, "RF and microwave high bandwidth signal processing based on Kerr Micro-combs", Advances in Physics X, VOL. 6, NO. 1, 1838946 (2021). DOI:10.1080/23746149.2020.1838946.

[136] X. Xu, et al., "Advanced RF and microwave functions based on an integrated optical frequency comb source," Opt. Express, vol. 26 (3) 2569 (2018).

[137] M. Tan, X. Xu, J. Wu, B. Corcoran, A. Boes, T. G. Nguyen, S. T. Chu, B. E. Little, R.Morandotti, A. Lowery, A. Mitchell, and D. J. Moss, ""Highly Versatile Broadband RF Photonic Fractional Hilbert Transformer Based on a Kerr Soliton Crystal Microcomb", Journal of Lightwave Technology vol. 39 (24) 7581-7587 (2021).

[138] X. Xu, M. Tan, J. Wu, T. Nguyen, S. Chu, B. Little, R. Morandotti, A. Mitchell, and D. Moss, "High performance RF filters via bandwidth scaling with Kerr micro-combs," APL Photonics, vol. 4, no. 2, pp. 1-8, 2019.

[139] M. Tan, et al., “Photonic RF arbitrary waveform generator based on a soliton crystal micro-comb source”, Journal of Lightwave Technology, vol. 38, no. 22, pp. 6221-6226, Oct 22. 2020. DOI: 10.1109/JLT.2020.3009655.

[140] M. Tan, X. Xu, J. Wu, R. Morandotti, A. Mitchell, and D. J. Moss, “RF and microwave high bandwidth signal processing based on Kerr Micro-combs”, Advances in Physics X, VOL. 6, NO. 1, 1838946 (2021). DOI:10.1080/23746149.2020.1838946.

[141] X. Xu, et al., “Advanced RF and microwave functions based on an integrated optical frequency comb source,” Opt. Express, vol. 26 (3) 2569 2018.

[142] L. Moura, “Radio Frequency Implementation of the Fractional Hilbert Transform with Transversal Filters,” Circuits, Systems & Signal Processing, vol. 26, pp. 407-417, 2007.

[143] A. W. Lohmann, D. Mendlovic, and Z. Zalevsky, “Fractional Hilbert transform,” Optics Letters, vol. 21, no. 4, pp. 281-283, 1996/02/15, 1996.

[144] A. D. Poularikas, A. F. Poularikas, and P. A. D, The Transforms and Applications Handbook: CRC-Press, 1996.

[145] V. K. Peddinti, and R. Kumaresan, “Bandpass phase shifter and analytic signal generator,” Signal Process., vol. 125, no. C, pp. 216–220, 2016.

[146] H. P. Bazargani, M. d. R. Fernández-Ruiz, and J. Azaña, “Tunable, nondispersive optical filter using photonic Hilbert transformation,” Optics Letters, vol. 39, no. 17, pp. 5232-5235, 2014/09/01, 2014.

[147] H. P. Bazargani, M. R. Fernández-Ruiz, and J. Azaña, "Tunable optical filter using photonic Hilbert transformation," OSA Technical Digest (online). p. SPM4D.6.

[148] T. G. Nguyen, M. Shoeiby, S. T. Chu, B. E. Little, R. Morandotti, A. Mitchell, and D. J. Moss, “Integrated frequency comb source based Hilbert transformer for wideband microwave photonic phase analysis,” Optics Express, vol. 23, no. 17, pp. 22087-22097, 2015/08/24, 2015.

[149] H. Emami, N. Sarkhosh, L. A. Bui, and A. Mitchell, “Wideband RF photonic in-phase and quadrature-phase generation,” Optics Letters, vol. 33, no. 2, pp. 98-100, 2008/01/15, 2008.

[150] M. Li, and J. Yao, “All-fiber temporal photonic fractional Hilbert transformer based on a directly designed fiber Bragg grating,” Optics Letters, vol. 35, no. 2, pp. 223-225, 2010/01/15, 2010.

[151] M. Li, and J. Yao, “Experimental Demonstration of a Wideband Photonic Temporal Hilbert Transformer Based on a Single Fiber Bragg Grating,” IEEE Photonics Technology Letters, vol. 22, no. 21, pp. 1559-1561, 2010.

[152] M. H. Asghari, and J. Azaña, “All-optical Hilbert transformer based on a single phase-shifted fiber Bragg grating: design and analysis,” Optics Letters, vol. 34, no. 3, pp. 334-336, 2009/02/01, 2009.

[153] T. Yang, J. Dong, L. Liu, S. Liao, S. Tan, L. Shi, D. Gao, and X. Zhang, “Experimental observation of optical differentiation and optical Hilbert transformation using a single SOI microdisk chip,” Scientific Reports, vol. 4, no. 1, pp. 3960, 2014/02/04, 2014.

[154] Z. Zhang, C. Sima, B. Liu, B. Cai, Y. Gao, M. Zhang, L. Shen, Y. Yu, M. Huang, Z. Lian, M. T. Posner, J. C. Gates, P. G. R. Smith, and D. Liu, “Wideband and continuously-tunable fractional photonic Hilbert transformer based on a single high-birefringence planar Bragg grating,” Optics Express, vol. 26, no. 16, pp. 20450-20458, 2018/08/06, 2018.

[155] C. Sima, J. C. Gates, C. Holmes, P. L. Mennea, M. N. Zervas, and P. G. R. Smith, “Terahertz bandwidth photonic Hilbert transformers based on synthesized planar Bragg grating fabrication,” Optics Letters, vol. 38, no. 17, pp. 3448-3451, 2013/09/01, 2013.

[156] L. Zhuang, M. R. Khan, W. Beeker, A. Leinse, R. Heideman, and C. Roeloffzen, “Novel microwave photonic fractional Hilbert transformer using a ring resonator-based optical all-pass filter,” Optics Express, vol. 20, no. 24, pp. 26499-26510, 2012/11/19, 2012.

[157] H. Shahoei, P. Dumais, and J. Yao, “Continuously tunable photonic fractional Hilbert transformer using a high-contrast germanium-doped silica-on-silicon microring resonator,” Optics Letters, vol. 39, no. 9, pp. 2778-2781, 2014/05/01, 2014.

[158] W. Liu, M. Li, R. S. Guzzon, E. J. Norberg, J. S. Parker, M. Lu, L. A. Coldren, and J. Yao, “A fully reconfigurable photonic integrated signal processor,” Nature Photonics, vol. 10, no. 3, pp. 190-195, 2016/03/01, 2016.

[159] Z. Li, Y. Han, H. Chi, X. Zhang, and J. Yao, “A Continuously Tunable Microwave Fractional Hilbert Transformer Based on a Nonuniformly Spaced Photonic Microwave Delay-Line Filter,” Journal of Lightwave Technology, vol. 30, no. 12, pp. 1948-1953, 2012/06/15, 2012.

[160] Z. Li, H. Chi, X. Zhang, and J. Yao, “A Continuously Tunable Microwave Fractional Hilbert Transformer Based on a Photonic Microwave Delay-Line Filter Using a Polarization Modulator,” IEEE Photonics Technology Letters, vol. 23, no. 22, pp. 1694-1696, 2011.

[161] Y. Park, M. H. Asghari, R. Helsten, and J. Azana, “Implementation of Broadband Microwave Arbitrary-Order Time Differential Operators Using a Reconfigurable Incoherent Photonic Processor,” IEEE Photonics Journal, vol. 2, no. 6, pp. 1040-1050, 2010.

[162] J. Feldmann, N. Youngblood, M. Karpov, H. Gehring, X. Li, M. Stappers, M. Le Gallo, X. Fu, A. Lukashchuk, A. S. Raja, J. Liu, C. D. Wright, A. Sebastian, T. J. Kippenberg, W. H. P. Pernice, and H.

Bhaskaran, “Parallel convolutional processing using an integrated photonic tensor core,” Nature, vol. 589, no. 7840, pp. 52-58, 2021/01/01, 2021.

[163] D. Marpaung, J. Yao, and J. Capmany, “Integrated microwave photonics,” Nature Photonics, vol. 13, no. 2, pp. 80-90, 2019/02/01, 2019.

[164] Z. Zhu, H. Chi, T. Jin, S. Zheng, X. Jin, and X. Zhang, “All-positive-coefficient microwave photonic filter with rectangular response,” Optics Letters, vol. 42, no. 15, pp. 3012-3015, 2017/08/01, 2017.

[165] R. A. Minasian, “Ultra-Wideband and Adaptive Photonic Signal Processing of Microwave Signals,” IEEE Journal of Quantum Electronics, vol. 52, no. 1, pp. 1-13, 2016.

[166] W. Wang, W. Zhang, Z. Lu, S. T. Chu, B. E. Little, Q. Yang, L. Wang, and W. Zhao, “Self-locked orthogonal polarized dual comb in a microresonator,” Photonics Research, vol. 6, no. 5, pp. 363-367, 2018/05/01, 2018.

[167] J. Capmany, J. Mora, I. Gasulla, J. Sancho, J. Lloret, and S. Sales, “Microwave Photonic Signal Processing,” Journal of Lightwave Technology, vol. 31, no. 4, pp. 571-586, 2013/02/15, 2013.

[168] R. A. Minasian, “Photonic signal processing of microwave signals,” IEEE Transactions on Microwave Theory and Techniques, vol. 54, no. 2, pp. 832-846, 2006.

[169] J. Capmany, and D. Novak, “Microwave photonics combines two worlds,” Nature Photonics, vol. 1, no. 6, pp. 319-330, 2007/06/01, 2007.

[170] R. Williamson, and R. D. Esman, “RF Photonics,” Journal of Lightwave Technology, vol. 26, no. 9, pp. 1145-1153, 2008/05/01, 2008.

[171] Y. Liu, J. Hotten, A. Choudhary, B. J. Eggleton, and D. Marpaung, “All-optimized integrated RF photonic notch filter,” Optics Letters, vol. 42, no. 22, pp. 4631-4634, 2017/11/15, 2017.

[172] C. Tseng, and S.-C. Pei, “Design and application of discrete-time fractional Hilbert transformer,” Circuits and Systems II: Analog and Digital Signal Processing, IEEE Transactions on, vol. 47, pp. 1529-1533, 01/01, 2001.

[173] J. A. Davis, D. E. McNamara, and D. M. Cottrell, “Analysis of the fractional Hilbert transform,” Appl. Opt., vol. 37, no. 29, pp. 6911-6913, Oct. 1998.

[174] C. D. Holdenried, J. W. Haslett, and B. Davies, “A fully integrated 10-Gb/s tapped delay Hilbert transformer for optical single sideband,” IEEE Microw. Wireless Compon. Lett., vol. 15, no. 5, pp. 303-305, May 2005.

[175] H. Emami, N. Sarkhosh, L. A. Bui, and A. Mitchell, “Wideband RF photonic in-phase and quadrature-phase generation,” Opt. Lett., vol. 33, no. 2, pp. 98-100, Jan 15. 2008.

[176] W. Liu, et al., "A Fully Reconfigurable Photonic Integrated Signal Processor," Nature Photonics, vol. 10, no. 3, pp. 190-196, 2016.

[177] F. Zeng, and J. Yao, “An Approach to Ultrawideband Pulse Generation and Distribution Over Optical Fiber,” IEEE Photonics Technol. Lett., vol. 18, no. 7, pp. 823-825, Apr. 2006.

[178] S. Pan, and J. Yao, “Optical generation of polarity- and shape-switchable ultrawideband pulses using a chirped intensity modulator and a first-order asymmetric Mach-Zehnder interferometer,” Opt. Lett., vol. 34, no. 9, pp. 1312-1314, May. 2009.

[179] Y. Yu, J. Dong, X. Li, and X. Zhang, “Ultra-Wideband Generation Based on Cascaded Mach-Zehnder Modulators,” IEEE Photonics Technol. Lett., vol. 23, no. 23, Dec. 2011.

[180] A. O.-Blanch, J. Mora, J. Capmany, B. Ortega, and D. Pastor, “Tunable radio-frequency photonic filter based on an actively mode-locked fiber laser,” Opt. Lett., vol. 31, no. 6, pp. 709-711, Mar. 2006.

[181] V. R. Supradeepa, C. M. Long, R. Wu. F. Ferdous, E. Hamidi, D. E. Leaird, and A. M. Weiner, “Comb-based radiofrequency photonic filters with rapid tunability and high selectivity,” Nature Photonics, vol. 6, pp. 186-194, Mar. 2012.

[182] V. T.-Company, and A. M. Weiner, “Optical frequency comb technology for ultra-broadband radio-frequency photonics,” Laser Photonics Rev., vol. 8, no. 3, pp. 368-393, 2014.

[183] Ghelfi, P., Laghezza, F., Scotti, F., Serafino, G., Capria, A., Pinna, S., Onori, D., Porzi, C., Scaffardi, M., Malacarne, A., Vercesi, V., Lazzeri, E., Berizzi, F., and Bogoni, A.: ‘A fully photonics-based coherent radar system’, Nature, 2014, vol. 507, (7492), pp. 341-345

[184] Skolnik, M.: ‘Role of radar in microwaves’, IEEE Transactions on Microwave Theory and Techniques, 2002, 50, (3), pp. 625-632

[185] Cundiff, S.T., and Weiner, A.M.: ‘Optical arbitrary waveform generation’, Nat. Photonics, 2010, 4, (11), pp. 760-766

[186] Rashidinejad, A., Li, Y., and Weiner, A.M.: ‘Recent Advances in Programmable Photonic-Assisted Ultrabroadband Radio-Frequency Arbitrary Waveform Generation’, IEEE Journal of Quantum Electronics, 2016, vol. 52, (1), pp. 1-17

[187] Ghelfi, P., Scotti, F., Laghezza, F., and Bogoni, A.: ‘Photonic Generation of Phase-Modulated RF Signals for Pulse Compression Techniques in Coherent Radars’, Journal of Lightwave Technology, 2012, vol. 30, (11), pp. 1638-1644

[188] Khan, M.H., Shen, H., Xuan, Y., Zhao, L., Xiao, S., Leaird, D.E., Weiner, A.M., and Qi, M.: 'Ultrabroad-bandwidth arbitrary radiofrequency waveform generation with a silicon photonic chip-based spectral shaper', Nat. Photonics, 2010, vol. 4, (2), pp. 117-122

[189] Chi, H., and Yao, J.: 'Photonic Generation of Phase-Coded Millimeter-Wave Signal Using a Polarization Modulator', IEEE Microwave and Wireless Components Letters, 2008, vol. 18, (5), pp. 371-373

[190] Zhang, Y., and Pan, S.: 'Generation of phase-coded microwave signals using a polarization-modulator-based photonic microwave phase shifter', Opt. Lett., 2013, vol. 38, (5), pp. 766-768

[191] Zhu, S., Shi, Z., Li, M., Zhu, N.H., and Li, W.: 'Simultaneous frequency upconversion and phase coding of a radio-frequency signal for photonic radars', Opt. Lett., 2018, vol. 43, (3), pp. 583-586

[192] Zhu, S., Li, M., Wang, X., Zhu, N.H., Cao, Z.Z., and Li, W.: 'Photonic generation of background-free binary phase-coded microwave pulses', Opt. Lett., 2019, vol. 44, (1), pp. 94-97

[193] Li, Z., Li, W., Chi, H., Zhang, X., and Yao, J.: 'Photonic generation of phase-coded microwave signal with large frequency tunability', IEEE Photonics Technology Letters, 2011, vol. 23, (11), pp. 712-714

[194] Liu, W., and Yao, J.: 'Photonic generation of microwave waveforms based on a polarization modulator in a Sagnac loop', Journal of Lightwave Technology, 2014, vol. 32, (20), pp. 3637-3644

[195] Wang, J., Shen, H., Fan, L., Wu, R., Niu, B., Varghese, L.T., Xuan, Y., Leaird, D.E., Wang, X., and Gan, F.: 'Reconfigurable radio-frequency arbitrary waveforms synthesized in a silicon photonic chip', Nat. Commun., 2015, 6, (1), pp. 1-8

[196] Ashrafi, R., Li, M., and Azaña, J.: 'Multi-TBaud optical coding based on superluminal space-to-time mapping in long period gratings', Optics and Photonics Journal, 2013, vol. 3, (2), pp. 126-130

[197] Rashidinejad, A., and Weiner, A.M.: 'Photonic radio-frequency arbitrary waveform generation with maximal time-bandwidth product capability', Journal of Lightwave Technology, 2014, 32, (20), pp. 3383-3393

[198] Jiang, Z., Huang, C.-B., Leaird, D.E., and Weiner, A.M.: 'Optical arbitrary waveform processing of more than 100 spectral comb lines', Nat. Photonics, 2007, vol. 1, (8), pp. 463-467

[199] Dai, Y., and Yao, J.: 'Microwave pulse phase encoding using a photonic microwave delay-line filter', Opt. Lett., 2007, vol. 32, (24), pp. 3486-3488

[200] S. Pan, J. Yao, "Optical generation of polarity- and shape-switchable ultrawideband pulses using a chirped intensity modulator and a first-order asymmetric Mach-Zehnder interferometer," Opt. Lett., vol. 34, no. 9, pp. 1312-1314, 2009.

[201] X. Li, J. Dong, Y. Yu, and X. Zhang, “A Tunable Microwave Photonic Filter Based on an All-Optical Differentiator,” IEEE Photon. Technol. Lett., vol. 23, no. 22, pp. 308-310, Mar. 2011.

[202] Y. Han, Z. Li, and J. Yao, “A Microwave Bandpass Differentiator Implemented Based on a Nonuniformly-Spaced Photonic Microwave Delay-Line Filter,” J. Lightw. Technol., vol. 29, no. 22, pp. 3470-3475, Nov. 2011.

[203] R. Ashrafı and J. Azaña, “Figure of merit for photonic differentiators,” Opt. Exp., vol. 20, no. 3, pp. 2626-2639, Jan. 2012.

[204] F. Zeng and J. Yao, “Ultrawideband Impulse Radio Signal Generation Using a High-Speed Electrooptic Phase Modulator and a Fiber-Bragg-Grating-Based Frequency Discriminator,” IEEE Photon. Technol. Lett., vol. 18, no. 19, pp. 2062-2064, Oct. 2006.

[205] P. Li, H. Chen, M. Chen, and S. Xie, “Gigabit/s Photonic Generation, Modulation, and Transmission for a Reconfigurable Impulse Radio UWB Over Fiber System,” IEEE Photon. Technol. Lett., vol. 4, no. 3, pp. 805-816, Jun. 2012.

[206] Y. Yu, F. Jiang, H. Tang, L. Xu, X. Liu, J. Dong, and X. Zhang, “Reconfigurable photonic temporal differentiator based on a dual-drive Mach-Zehnder modulator,” Opt. Exp., vol. 24, no. 11, pp. 11739-11748, May 2016.

[207] P. Velanas, A. Bogris, A. Argyris, and D. Syvridis, “High-Speed All-Optical First- and Second-Order Differentiators Based on Cross-Phase Modulation in Fibers,” J. Lightw. Technol., vol. 26, no. 18, pp. 3269-3276, Sep. 2008.

[208] J. Xu, X. Zhang, J. Dong, D. Liu, and D. Huang, “All-optical differentiator based on cross-gain modulation in semiconductor optical amplifier,” Opt. Lett., vol. 32, no. 20, pp. 3029-3031, Oct. 2007.

[209] J. Xu, X. Zhang, J. Dong, D. Liu, and D. Huang, “High-speed all-optical differentiator based on a semiconductor optical amplifier and an optical filter,” Opt. Lett., vol. 32, no. 13, pp. 1872-1874, Jul. 2007.

[210] F. Wang, J. Dong, E. Xu, and X. Zhang, “All-optical UWB generation and modulation using SOA-XPM effect and DWDM-based multi-channel frequency discrimination,” Opt. Exp., vol. 18, no. 24, pp. 24588-24594, Nov. 2010.

[211] V. Moreno, M. Rius, J. Mora, M. A. Muriel, and J. Capmany, “Integrable high order UWB pulse photonic generator based on cross phase modulation in a SOA-MZI,” Opt. Exp., vol. 21, no. 19, pp. 22911-22917, Sep. 2013.

[212] Q. Wang and J. Yao, “Switchable optical UWB monocycle and doublet generation using a reconfigurable photonic microwave delay-line filter,” Opt. Exp., vol. 15, no. 22, pp. 14667-14672, Oct. 2007.

[213] M. Bolea, J. Mora, B. Ortega, and J. Capmany, “Optical UWB pulse generator using an N tap microwave photonic filter and phase inversion adaptable to different pulse modulation formats,” Opt. Exp., vol. 17, no. 7, pp. 5023-50332, Mar. 2009.

[214] B. Mathieu, P. Melchior, A. Oustaloup, C. Ceyral, “Fractional differentiation for edge detection,” Signal Processing, vol. 83, pp. 2421-2432, Nov. 2003.

[215] A. Oustaloup, F. Levron, B. Mathieu, and F. M. Nanot, “Frequency-Band Complex Noninteger Differentiator: Characterization and Synthesis,” IEEE Trans. on Circuit and Systems - I: Fundamental Theory and Application, vol. 47, no. 1, pp. 25-39, Jan. 2000.

[216] F. Li, Y. Park, and J. Azaña, “Linear Characterization of Optical Pulses With Durations Ranging From the Picosecond to the Nanosecond Regime Using Ultrafast Photonic Differentiation,” J. Lightw. Technol., vol. 27, no. 1, pp. 4623-4633, 2009.

[217] Stern, B., Ji, X., Okawachi, Y., Gaeta, A. L. & Lipson, M. Battery-operated integrated frequency comb generator. Nature 562, 401 (2018).

[218] Bao, C., et al., Direct soliton generation in microresonators, Opt. Lett, vol. 42, 2519 (2017).

[219] M.Ferrera et al., “CMOS compatible integrated all-optical RF spectrum analyzer”, Optics Express, vol. 22, no. 18, 21488 - 21498 (2014).

[220] A. Pasquazi, et al., “Sub-picosecond phase-sensitive optical pulse characterization on a chip”, Nature Photonics, vol. 5, no. 10, pp. 618-623 (2011).

[221] M. Kues, et al., “Passively modelocked laser with an ultra-narrow spectral width”, Nature Photonics, vol. 11, no. 3, pp. 159, 2017.

[222] H Bao, L Olivieri, M Rowley, ST Chu, BE Little, R Morandotti, DJ Moss, ... “Turing patterns in a fiber laser with a nested microresonator: Robust and controllable microcomb generation”, Physical Review Research vol. 2 (2), 023395 (2020).

[223] Little, B. E. et al., “Very high-order microring resonator filters for WDM applications”, IEEE Photonics Technol. Lett. vol. 16, 2263–2265 (2004).

[224] Bao, C., et al., Direct soliton generation in microresonators, Opt. Lett, vol. 42, 2519 (2017).

[225] M.Ferrera et al.“On-Chip ultra-fast 1st and 2nd order CMOS compatible all-optical integration”, Opt. Express, vol. 19, (23) pp. 23153-23161 (2011).

[226] H Bao, L Olivieri, M Rowley, ST Chu, BE Little, R Morandotti, DJ Moss, ... “Turing patterns in a fiber laser with a nested microresonator: Robust and controllable microcomb generation”, Physical Review Research vol. 2 (2), 023395 (2020).

[227] M. Ferrera, et al., “On-chip CMOS-compatible all-optical integrator”, Nature Communications, vol. 1, Article 29, 2010.

[228] M. Ferrera et al., “Low Power CW Parametric Mixing in a Low Dispersion High Index Doped Silica Glass Micro-Ring Resonator with Q-factor > 1 Million”, Optics Express, vol.17, no. 16, pp. 14098–14103 (2009).

[229] A. Pasquazi, et al., “Self-locked optical parametric oscillation in a CMOS compatible microring resonator: a route to robust optical frequency comb generation on a chip,” Optics Express, vol. 21, no. 11, pp. 13333-13341, 2013.

[230] A. Pasquazi, et al., “Stable, dual mode, high repetition rate mode-locked laser based on a microring resonator,” Optics Express, vol. 20, no. 24, pp. 27355-27362, 2012.

[231] Bao, C., et al., Direct soliton generation in microresonators, Opt. Lett, 42, 2519 (2017).

[232] A. Frigg, A. Boes, G. Ren, T.G. Nguyen, D.Y. Choi, S. Gees, D. Moss, A Mitchell, “Optical frequency comb generation with low temperature reactive sputtered silicon nitride waveguides”, APL Photonics, Vol. 5 (1), 011302 (2020).

[233] M. Ferrera, et al., “On-chip CMOS-compatible all-optical integrator”, Nature Communications, vol. 1, Article 29, 2010.

[234] A. Pasquazi, Y. Park, J. Azaña, F. Légaré, R. Morandotti, B. E. Little, S. T. Chu, and D. J. Moss, “Efficient wavelength conversion and net parametric gain via Four Wave Mixing in a high index doped silica waveguide,” Optics Express, vol. 18, no. 8, pp. 7634-7641, 2010/04/12, 2010.

[235] A. Pasquazi, Y. Park, J. Azana, et al., “Efficient wavelength conversion and net parametric gain via Four Wave Mixing in a high index doped silica waveguide,” Optics Express, vol. 18, no. 8, pp. 7634-7641, 2010.

[236] A. Pasquazi, et al., “All-optical wavelength conversion in an integrated ring resonator,” Optics Express, vol. 18 (4) 3858 (2010).

[237] M. Peccianti, M. Ferrera, L. Razzari, et al., “Subpicosecond optical pulse compression via an integrated nonlinear chirper,” Optics Express, vol. 18, no. 8, pp. 7625-7633, 2010.

[238] A. Pasquazi, et al., “Sub-picosecond phase-sensitive optical pulse characterization on a chip”, Nature Photonics, vol. 5, no. 10, pp. 618-623 (2011).

[239] M. Kues, et al., “Passively modelocked laser with an ultra-narrow spectral width”, Nature Photonics, vol. 11, no. 3, pp. 159, 2017.

[240] Kues, M. et al. "Quantum optical microcombs". Nature Photonics vol. 13, (3) 170-179 (2019). doi:10.1038/s41566-019-0363-0

[241] P. Roztocki et al., “Complex quantum state generation and coherent control based on integrated frequency combs”, Journal of Lightwave Technology vol. 37 (2) 338-347 (2019).

[242] S. Sciara et al., “Generation and Processing of Complex Photon States with Quantum Frequency Combs”, IEEE Photonics Technology Letters vol. 31 (23) 1862-1865 (2019). DOI: 10.1109/LPT.2019.2944564.

[243] L. Caspani, C. Reimer, M. Kues, et al., “Multifrequency sources of quantum correlated photon pairs on-chip: a path toward integrated Quantum Frequency Combs,” Nanophotonics, vol. 5, no. 2, pp. 351-362, 2016.

[244] C. Reimer, L. Caspani, M. Clerici, et al., “Integrated frequency comb source of heralded single photons,” Optics Express, vol. 22, no. 6, pp. 6535-6546, 2014.

[245] C. Reimer, et al., “Cross-polarized photon-pair generation and bi-chromatically pumped optical parametric oscillation on a chip”, Nature Communications, vol. 6, Article 8236, 2015. DOI: 10.1038/ncomms9236.

[246] C. Reimer et al., “Generation of multiphoton entangled quantum states by means of integrated frequency combs,” Science, vol. 351, no. 6278, pp. 1176-1180, 2016.

[247] M. Kues, et al., “On-chip generation of high-dimensional entangled quantum states and their coherent control”, Nature, vol. 546, no. 7660, pp. 622-626, 2017.

[248] Y. Zhang, et al., “Induced photon correlations through superposition of two four-wave mixing processes in integrated cavities”, Laser and Photonics Reviews, vol. 14, no. 7, pp. 2000128, 2020. DOI: 10.1002/lpor.202000128

[249] P. Roztocki et al., “Practical system for the generation of pulsed quantum frequency combs,” Optics Express, vol. 25, no. 16, pp. 18940-18949, 2017.

[250] Y. Zhang, et al., “Induced photon correlations through superposition of two four-wave mixing processes in integrated cavities”, Laser and Photonics Reviews, vol. 14, no. 7, pp. 2000128, 2020. DOI: 10.1002/lpor.202000128

[251] C. Reimer, et al.,“High-dimensional one-way quantum processing implemented on d-level cluster states”, Nature Physics, vol. 15, no.2, pp. 148–153, 2019.

Figures

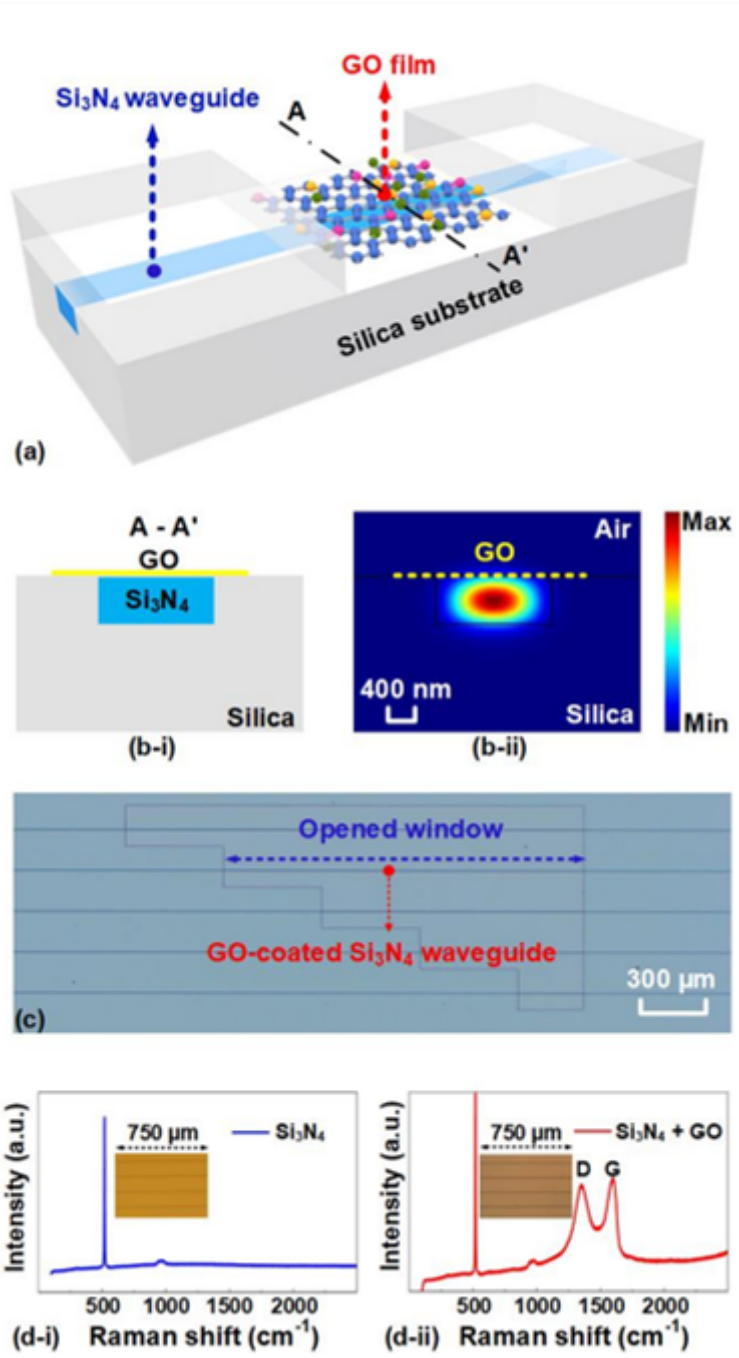

Figure 1

(a) Schematic illustration of a GO-coated Si_3N_4 waveguide with a monolayer GO film. (b-i) Schematic illustration of cross section and (b-ii) corresponding TE mode profile of the GO-coated Si_3N_4 waveguide in (a). (c) Microscope image of a Si_3N_4 integrated chip uniformly coated with monolayer GO film. (d) Raman spectra of a Si_3N_4 chip (i) before and (ii) after coating 2 layers of GO. Insets show the corresponding microscope images.

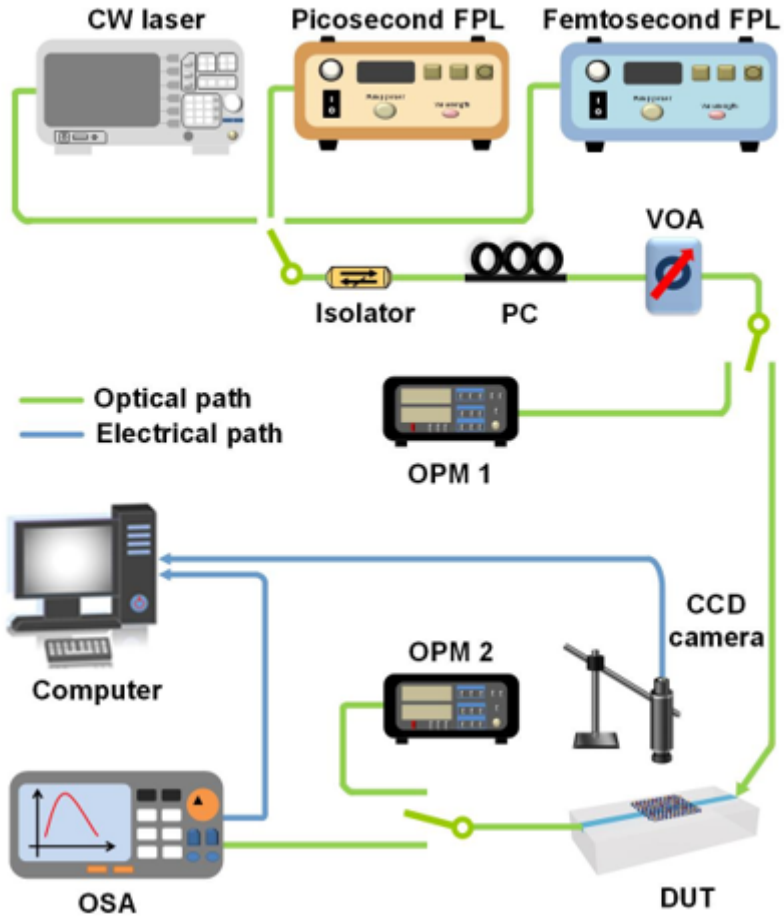

Figure 2

Experimental setup for measuring loss and SPM of GO-coated Si_3N_4 waveguides. CW laser: continuous-wave laser. FPL: fiber pulsed laser. PC: polarization controller. VOA: variable optical attenuator. OPM: optical power meter. DUT: device under test. CCD: charged-coupled device. OSA: optical spectrum analyzer.

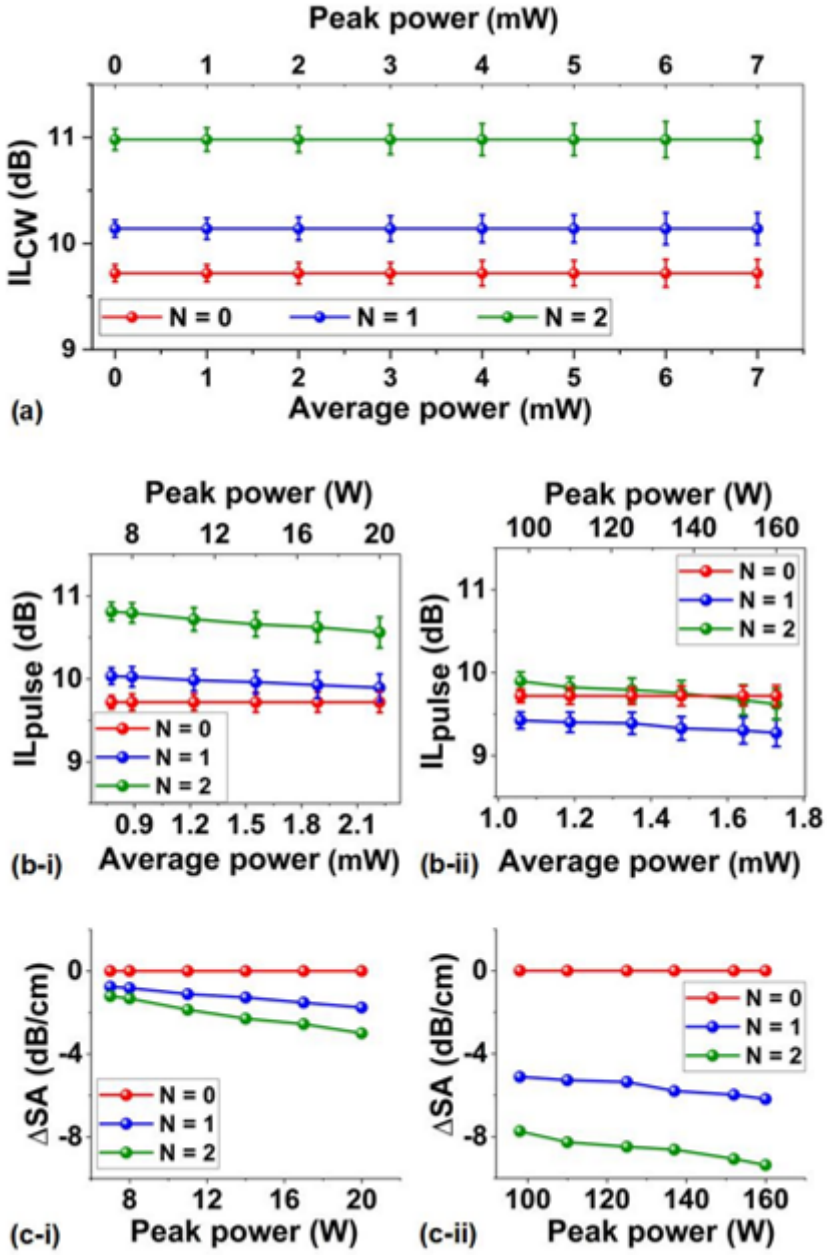

Figure 3

(a) Measured insertion loss (IL_{CW}) of GO-coated Si_3N_4 waveguides versus input power of continuous-wave (CW) light. (b) Measured insertion loss (IL_{pulse}) of GO-coated Si_3N_4 waveguides versus input power of optical pulses. (c) Excess propagation loss induced by the SA (ΔSA) versus peak power of input optical pulses. In (b) and (c), (i) and (ii) show the results for picosecond and femtosecond optical pulses, respectively. In (a) – (c), the results for uncoated ($N = 0$) and hybrid Si_3N_4 waveguides coated with 1 and 2 layers of GO ($N = 1, 2$) are shown for comparison. The data points depict the average of measurements on three samples and the error bars illustrate the variations among the different samples.

Figure 4

SPM experimental results using picosecond optical pulses. (a) Normalized spectra of optical pulses before and after propagation through the GO-coated Si_3N_4 waveguides with 1 and 2 layers of GO at an input peak power of ~20 W. (b) Optical spectra measured at different input peak powers for the hybrid waveguides with 2 layers of GO. (c) BFs of the measured output spectra versus input peak power for the hybrid waveguides with 1 and 2 layers of GO. In (a) and (c), the corresponding results for the uncoated Si_3N_4 waveguides are also shown for comparison.

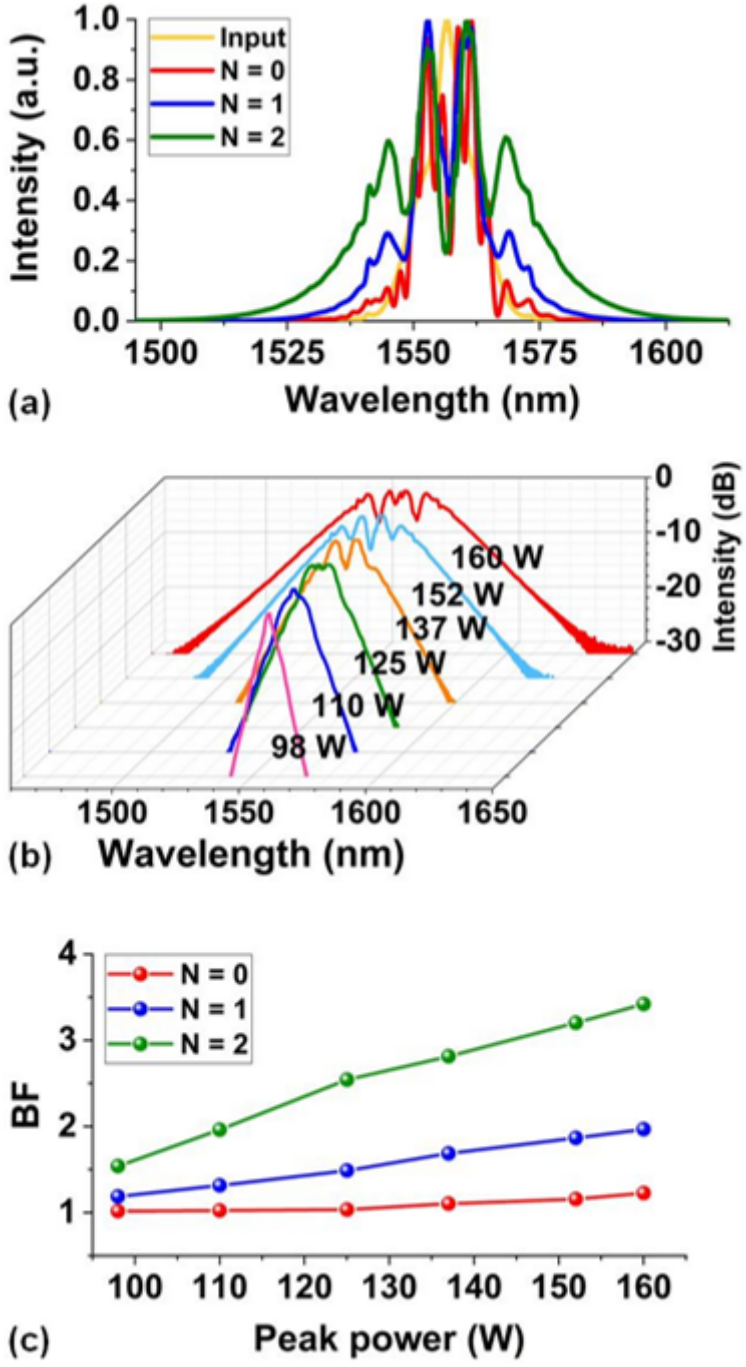

Figure 5

SPM experimental results using femtosecond optical pulses. (a) Normalized spectra of optical pulses before and after propagation through the GO-coated Si_3N_4 waveguides with 1 and 2 layers of GO at an input peak power of ~160 W. (b) Optical spectra measured at different input peak powers for the hybrid waveguides with 2 layers of GO. (c) BFs of the measured output spectra versus input peak power for the hybrid waveguides with 1 and 2 layers of GO. In (a) and (c), the corresponding results for the uncoated Si_3N_4 waveguides are also shown for comparison

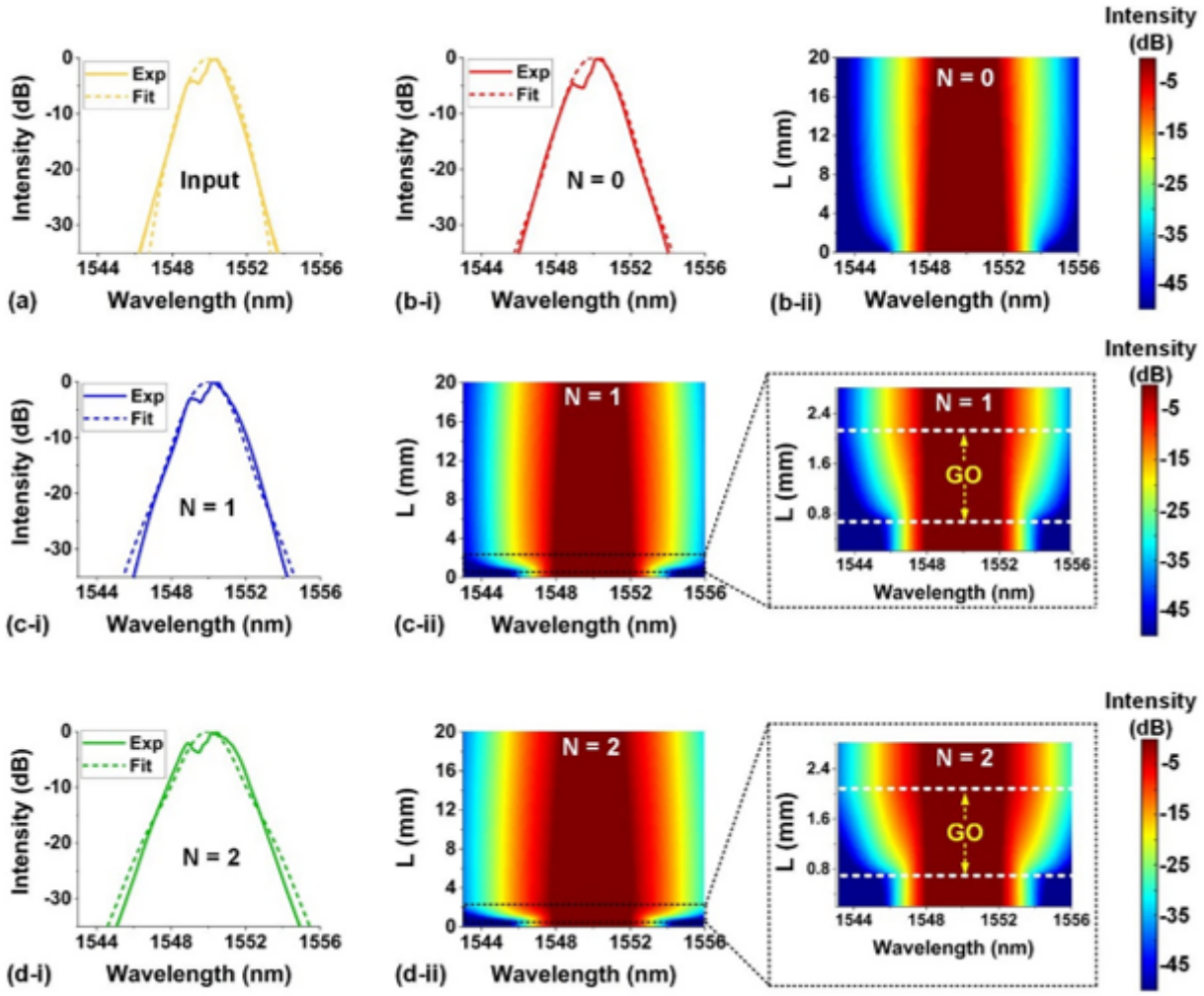

Figure 6

(a) Measured and fit spectra of input picosecond optical pulses. (b-i) Measured and fit output spectra after propagation through the uncoated Si_3N_4 waveguides. (b-ii) Simulated spectra evolution along the uncoated Si_3N_4 waveguide. (c-i) Measured and fit output spectra after propagation through the hybrid waveguide with 1 layer of GO. (c-ii) Simulated spectra evolution along the hybrid waveguide with 1 layer of GO. (d-i) Measured and fit output spectra after propagation through the hybrid waveguide with 2 layers of GO. (d-ii) Simulated spectra evolution along the hybrid waveguide with 2 layers of GO. Insets in (c-ii) and (d-ii) show zoom-in views for the GO-coated regions. In (b) – (d), the peak power of the input picosecond pulses is ~20 W.

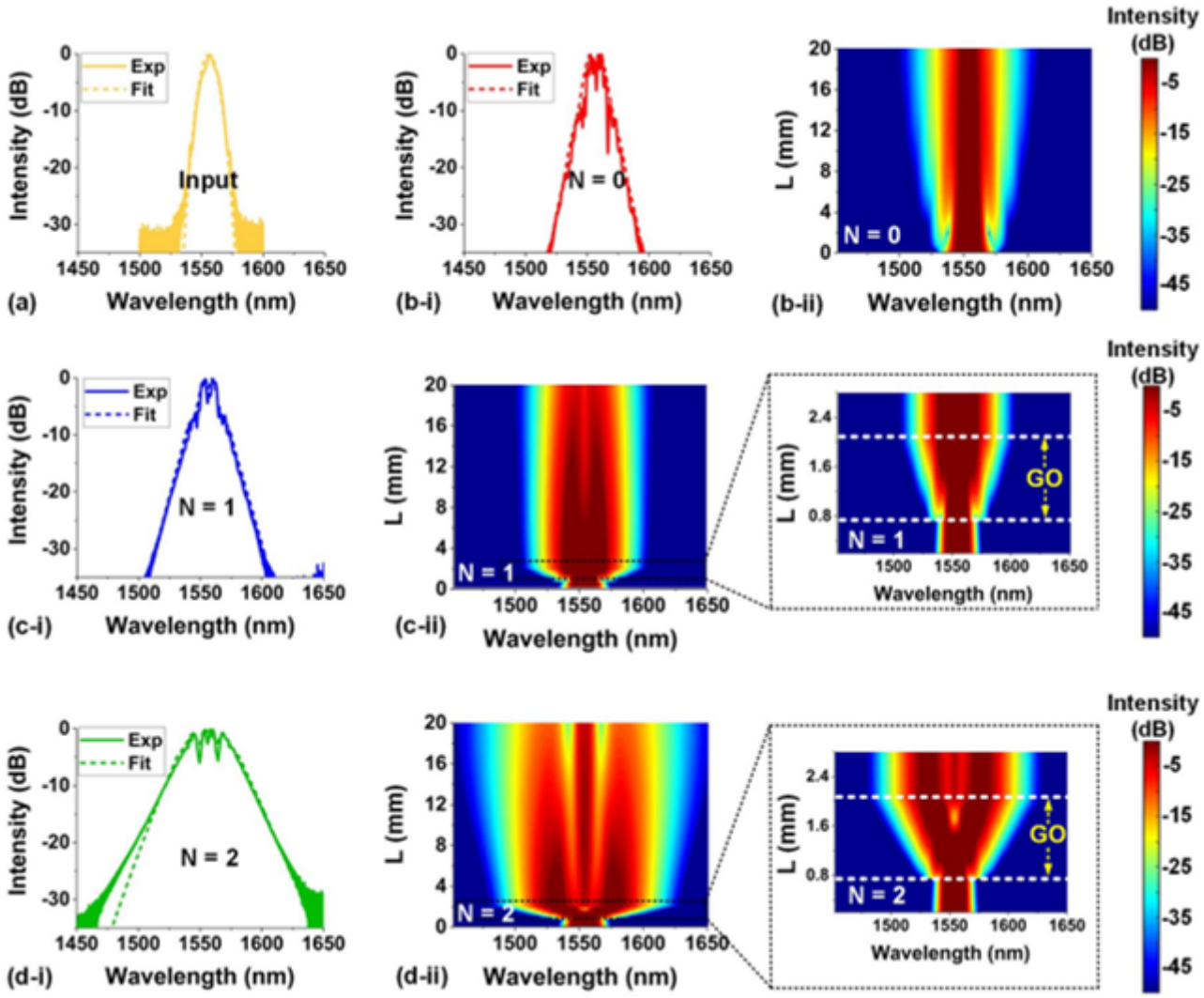

Figure 7

(a) Measured and fit spectra of input femtosecond optical pulses. (b-i) Measured and fit output spectra after propagation through the uncoated Si_3N_4 waveguides. (b-ii) Simulated spectra evolution along the uncoated Si_3N_4 waveguide. (c-i) Measured and fit output spectra after propagation through the hybrid waveguide with 1 layer of GO. (c-ii) Simulated spectra evolution along the hybrid waveguide with 1 layer of GO. (d-i) Measured and fit output spectra after propagation through the hybrid waveguide with 2 layers of GO. (d-ii) Simulated spectra evolution along the hybrid waveguide with 2 layers of GO. Insets in (c-ii) and (d-ii) show zoom-in views for the GO-coated regions. In (b) – (d), the peak power of the input femtosecond pulses is ~160 W.

Figure 8

(a) BFs versus GO film length (L_c) and input peak power (P_{peak}) for picosecond optical pulses after propagation through the hybrid waveguides. (b) BFs versus L_c and P_{peak} for femtosecond optical pulses after propagation through the hybrid waveguides. (c) BFs versus GO coating position (L_0) and P_{peak} for picosecond optical pulses after propagation through the hybrid waveguides. (d) BFs versus L_0 and P_{peak} for femtosecond optical pulses after propagation through the hybrid waveguides. In (a) – (d), (i) and (ii) show the corresponding results for the waveguides with 1 and 2 layers of GO, the black points mark the results corresponding to the device parameters and input powers in Figs. 4(a) and 5(a). In (a) and (b), L_0 = 0.7 mm. In (c) and (d), L_c = 1.4 mm.

Figure 9

(a) Comparison of spectral broadening of picosecond optical pulses after propagation through the GO-Si_3N_4 waveguide with and without considering the SA of GO. (b) Comparison of spectral broadening of femtosecond optical pulses after propagation through the GO-Si_3N_4 waveguide with and without considering the SA of GO. In (a) and (b), N = 2, L_c = 1.4 mm, and L_0 = 0.7 mm. The peak power for the picosecond and femtosecond optical pulses are 20 W and 160 W, respectively.